Journal of Computational Physics 255 (2013) 106–129

Contents lists available at ScienceDirect

Journal of Computational Physics

www.elsevier.com/locate/jcp

# On the remedy against shock anomalies in kinetic schemes

Taku Ohwada [a,*], Ryo Adachi [a], Kun Xu [b], Jun Luo [b]

[a] Department of Aeronautics and Astronautics, Graduate School of Engineering, Kyoto University, Kyoto 606-8501, Japan
[b] Department of Mathematics, Hong Kong University of Science and Technology, Clear Water Bay, Kowloon, Hong Kong

ARTICLE INFO

*Article history:*
Received 20 November 2012
Received in revised form 17 June 2013
Accepted 29 July 2013
Available online 13 August 2013

*Keywords:*
Carbuncle phenomenon
Post-shock oscillations
Shock-capturing
Kinetic scheme
Compressible Euler
Compressible Navier–Stokes
Blunt body
Aerodynamic heating

ABSTRACT

Shock-capturing schemes often exhibit anomalous behaviors, such as the carbuncle phenomenon and the post-shock oscillations, especially in the hypersonic flow regime. This paper proposes a simple and effective remedy against these shock instabilities in the case of the kinetic Lax–Wendroff scheme, where the well-known classic scheme is reinforced by means of an equilibrium distribution function of gas molecules. The pathologies are significantly improved to an acceptable level for practical purposes without any considerable side-effect by locally bringing out the robustness of the equilibrium flux method from the kinetic scheme. The remedy is applied only to the preprocessing of the data at cell-edges. The performance of the fortified kinetic scheme is demonstrated in the problem of a hypersonic inviscid or viscous flow past a blunt body. Comparisons are also made with various advanced shock-capturing schemes at present.



## 1. Introduction

Shock-capturing schemes for the compressible Euler equations have been earnestly studied by plenty of researchers since the 1970s and a lot of advanced schemes are now available. It sounds, nevertheless, a bit too exaggerative to say that the shock-capturing technology presently available is well-matured; even the most advanced schemes at present still exhibit anomalous behaviors which should not be overlooked. The carbuncle phenomenon is one of the representative pathologies and many studies have been devoted to the prevention and the cure against it, see e.g. Refs. [1–12] and the references therein. The occurrence of appreciable distortion behind a strong shock wave and the deformation of the shock wave, which sometimes appears in a crooked shape, are cited as its symptoms. This catastrophic pathology is said to be intrinsic to the compressible Euler equations [3,8]. It is not, however, peculiar to the computation of inviscid flows and physical dissipation often fails to prevent it. For example, the reliability of the CFD prediction of aerodynamic heating of a blunt body flying at a hypersonic speed, such as a spacecraft and a meteorite during atmospheric entry, is considerably deteriorated by the onset of the pathology. Besides, the bow shock in front of the body often generates numerical disturbances, i.e. the post-shock oscillations [13], and they can also affect the downstream boundary-layer, where the temperature gradient is extremely steep. These shock instabilities degrade the quality of computations of various shock-wave phenomena, such as shock-acoustic and shock-vortex interactions, transition to turbulence behind a shock wave, and so on.

The shock-capturing strategy, which was discovered by Godunov more than half a century ago [14], is now adopted in various numerical schemes. When the distribution of a numerical solution is reconstructed from its discrete data, discontinuities are intentionally introduced at cell-edges. A state is determined at each cell-edge as the solution of the corresponding Riemann problem and the numerical flux for the state is accompanied by numerical dissipation, which is effective for the

* Corresponding author.
*E-mail address:* ohwada@kuaero.kyoto-u.ac.jp (T. Ohwada).

0021-9991/$ – see front matter 
http://dx.doi.org/10.1016/j.jcp.2013.07.038

suppression of the occurrence of spurious oscillations around shocks. An excess of numerical dissipation, however, smears the numerical solution and its amount is cleverly controlled by a sophisticated method for preprocessing, such as MUSCL, ENO, WENO, and so forth, where high order accuracy with respect to space is retained except around shock waves. Ruminating about what Riemann solvers essentially do, we immediately notice or realize again Riemann solvers as the tools for the production of numerical dissipation. The simple arithmetic mean leads to a classical non-shock-capturing scheme and the nonlinearity in the averaging is of crucial importance. Without a priori knowledge of the explicit numerical dissipation desirable for shock-capturing, good tools for dissipation production are obtained only by empirical approaches. While mathematical theories are available for some simple cases, such as scalar conservation laws and 1st order accurate schemes for one space dimension, practitioners involved in projects of engineering or physics still have to resort to empiricism, in particular when they encounter the abovementioned shock anomalies. All efforts for high order accuracy are reduced to ashes in the presence of shock instabilities. Under such situations, there is no rational reason to hesitate to look for tools other than Riemann-solvers.

From the two elementary facts that (i) the compressible Euler equations describe the dynamical behavior of a gas in a local equilibrium state and (ii) the velocity distribution of gas molecules in an equilibrium state is given by the Maxwell distribution function (Maxwellian), we immediately recognize that Maxwellian yields the flux functions for the compressible Euler equations. This allows us to employ Maxwellian as a gadget for computing the average of two states in shock-capturing schemes. The equilibrium flux method (EFM) of Pullin [15], which is one of the originals of kinetic schemes, employs the same piecewise constant reconstruction as in Godunov's method. The numerical flux at a cell-edge is computed from the discontinuous distribution of gas molecules arriving from the two equilibrium states on both sides of the cell-edge, say the discontinuous Maxwellian. The noteworthy feature of EFM is found in its robustness; EFM is more robust than Godunov's method owing to the numerical dissipation generated by the discontinuous Maxwellian. At the same time EFM is too diffusive and is far from boundary-layer capturing. This drawback is partially resolved in the spatially high order accurate treatment, i.e. the kinetic flux vector splitting scheme (KFVS) [16], where a conventional method for high order accurate preprocessing, such as MUSCL, is introduced and the time variation of the numerical flux is taken into account by using the collisionless Boltzmann equation. Although KFVS (or the second order accurate EFM) can capture shock waves more sharply than the original EFM, however, the time variation of the numerical solution is not consistent with that of the compressible Euler equations up to second order accuracy.

The consistent accuracy with respect to time can be achieved by taking account of a more realistic or physical process with molecular collisions and the gas kinetic BGK scheme (GKB) has been developed along the lines [17,18]. GKB is the first kinetic scheme which combines the capability of shock-capturing and that of boundary-layer-capturing. The latter feature is in contrast to KFVS, which requires a prohibitively large number of mesh points in a boundary-layer as well as a very small time step for its accurate computation [17,19]. The fidelity to the real physics is not, however, the key ingredient of GKB, although it brings high order accuracy in time as the consequence. The key lies in the approximation of the Maxwellian which is employed as the distribution of gas molecules after collisions (the gain term in the BGK approximation). The solution of the BGK equation, on which GKB relies, consists of the initial data and the integral of the gain term along its characteristics (the method of integration factor). The discontinuous Maxwellian is employed in the former and the latter is approximated by using the continuous Maxwellian made from the discontinuous one, which is loyal to the BGK equation. The continuous Maxwellian also generates numerical dissipation but it is less dissipative than the discontinuous one. This immediately makes us recall the analogy to hybrid schemes, such as that of HLLE [21,22] and HLLC [23,24]; the former is dissipative and robust and the latter is less dissipative and works better in smooth regions. In Ref. [20], the classic Lax–Wendroff scheme is reinforced by exploiting these two kinetic averages and the resulting scheme, which will be hereafter called the kinetic Lax–Wendroff scheme (KLW), is shown to be able to cope with GKB.

While the abovementioned efforts have bestowed sophistication upon kinetic schemes, the robustness of the original has been lost; both GKB and KLW are afflicted with shock anomalies. Degeneracy does not, however, necessarily mean the loss of gene. In fact, these two kinetic schemes can vary from a Lax–Wendroff type scheme to EFM depending on the data at cell-edges. It is expected that the robustness of these schemes against shock instabilities is easily fortified without any additive dissipation only by a simple modification of the preprocessing to promote the transformation into EFM around shock waves. In the present study we will establish the authenticity of this prescription. Since the structure of KLW is simpler than that of GKB, we will mainly explain the case of KLW. The rest of the paper proceeds as follows. Section 2 briefly describes the derivation of KLW. Section 3 describes the diagnosis of the flaws of KLW. Section 4 explains the modification of the preprocessing. Its efficacy is confirmed in some preliminary problems. The performance of KLW with the remedy is examined in Section 5. A similar remedy is also applied to GKB and its effect is confirmed there. Some concluding remarks are presented in Section 6, where the essential role of kinetic theory for the robustness of kinetic schemes is discussed. Comparisons are also made with various advanced shock-capturing schemes at present in Sections 4 and 5.

## 2. Kinetic Lax–Wendroff scheme

The derivation of KLW in Ref. [20] does not impose any special prerequisites on the reader. It will be briefly reviewed here in order to keep this paper self-contained. In the following explanation, the 2D compressible Euler equations for a monatomic ideal gas will be considered. The generalization to 3D case can be made straightforwardly. The extension to the case of the Navier–Stokes equations for general ideal gases will be also mentioned.

### 2.1. Notation

In the present paper, all the explanations are given by using nondimensional variables. Time and rectangular space coordinates are denoted by $t$ and $(x, y, z)$, respectively. The density, the components of flow velocity in the $x$, $y$, $z$ directions, and the temperature of the gas are denoted by $\rho$, $u$, $v$, $w$, and $T$, respectively. These gas-dynamic variables, called the primitive variables, will be often denoted by $h_i$ $(i = 1, \ldots, 5)$ $(h_1 = \rho, \ldots, h_5 = T)$ or the vector $\boldsymbol{h}$ for concise expression. The conservative variables $\rho$, $\rho u$, $\rho v$, $\rho w$, $\rho(3T + u^2 + v^2 + w^2)/2$ will be also written as $\tilde{h}_i$ $(i = 1, \ldots, 5)$ or $\tilde{\boldsymbol{h}}$. The pressure of the gas is denoted by $P$. The components of the molecular velocity in the $x$, $y$, and $z$ directions are denoted by $\zeta_x$, $\zeta_y$, and $\zeta_z$, respectively. The distribution function of gas molecules in spatially 2D case is a function of $x$, $y$, $t$, $\zeta_x$, $\zeta_y$, and $\zeta_z$ and it is expressed as $f(x, y, t, \zeta_x, \zeta_y, \zeta_z)$. Incidentally, the explanations can be regarded as those for dimensional variables if $T$ is replaced by $RT$, where $R$ is the gas constant per unit mass.

### 2.2. Basic equations

The nondimensional compressible Euler equations are concisely written as

$$\frac{\partial \tilde{\boldsymbol{h}}}{\partial t} + \frac{\partial \boldsymbol{\Phi}}{\partial x} + \frac{\partial \boldsymbol{\Psi}}{\partial y} = 0, \tag{1}$$

where $\boldsymbol{\Phi}$ and $\boldsymbol{\Psi}$ are the flux vectors, each component of which is a function of the primitive variables $\boldsymbol{h}$ (or the conservative variables $\tilde{\boldsymbol{h}}$), i.e. $\boldsymbol{\Phi}(\boldsymbol{h})$. The pressure $P$ is defined by the equation of state

$$P = \rho T, \tag{2}$$

and is incorporated in the functional forms of the flux vectors.

### 2.3. Kinetic theory minimum

The kinetic theory tools which are necessary and sufficient for the derivation of KLW are summarized below.

(i) The distribution function $f(x, y, t, \zeta_x, \zeta_y, \zeta_z)$ yields the conservative variables $\tilde{\boldsymbol{h}}(x, y, z, t)$ as the moments

$$\tilde{\boldsymbol{h}} = \int_{R^3} \boldsymbol{\phi} f \, d\zeta_x \, d\zeta_y \, d\zeta_z, \tag{3}$$

where $\boldsymbol{\phi} = (\phi_1, \phi_2, \phi_3, \phi_4, \phi_5)^{\mathrm{T}} = (1, \zeta_x, \zeta_y, \zeta_z, (\zeta_x^2 + \zeta_y^2 + \zeta_z^2)/2)^{\mathrm{T}}$ and the domain of the integration is the whole molecular velocity space $R^3$.

(ii) The equilibrium distribution function $g$, which is a function of $\boldsymbol{h}(x, y, z, t)$, $\zeta_x$, $\zeta_y$, and $\zeta_z$, i.e. $g(\boldsymbol{h}(x, y, z, t), \zeta_x, \zeta_y, \zeta_z)$, yields $\tilde{\boldsymbol{h}}(x, y, z, t)$ as the same moments

$$\tilde{\boldsymbol{h}} = \int_{R^3} \boldsymbol{\phi} g \, d\zeta_x \, d\zeta_y \, d\zeta_z. \tag{4}$$

(iii) The $g$ yields the flux vectors for the compressible Euler equations:

$$\begin{pmatrix} \boldsymbol{\Phi} \\ \boldsymbol{\Psi} \end{pmatrix} = \int_{R^3} \boldsymbol{\phi} \begin{pmatrix} \zeta_x \\ \zeta_y \end{pmatrix} g \, d\zeta_x \, d\zeta_y \, d\zeta_z. \tag{5}$$

Maxwellian $f_M$, which is defined by

$$f_M = \frac{\rho}{(2\pi T)^{3/2}} \exp\left( -\frac{(\zeta_x - u)^2 + (\zeta_y - v)^2 + (\zeta_z - w)^2}{2T} \right), \tag{6}$$

is the classic equilibrium distribution function in kinetic theory and is adopted as $g$ in the present study, i.e. $g = f_M$. For artificial equilibrium distribution functions, see e.g. Ref. [20] (the compressible Euler equations) and Ref. [26] (scalar conservation laws).

### 2.4. Finite volume Lax–Wendroff method

The kinetic scheme reviewed here is categorized into the finite volume method. We will explain only about the computation of the numerical flux. For the details of the finite volume method for gas-dynamic equations, see e.g. Ref. [25]. Since gas-dynamic equations are rotation invariant, it suffices to consider only the case where the normal vector of a cell-edge is in the $x$ direction.

The numerical flux vector $\boldsymbol{F}$ is defined as the integral of the flux vector $\boldsymbol{\Phi}$ over the time step $\Delta t$:

$$\boldsymbol{F} = \int_0^{\Delta t} \boldsymbol{\Phi}\big(\boldsymbol{h}(t,\ldots)\big)\,dt. \tag{7}$$

It is evaluated at the middle point of each cell-edge, which results in second order accuracy in space when the integrand $\boldsymbol{\Phi}$ is appropriately approximated. The integrand $\boldsymbol{\Phi}$ is expanded around $t=0$ and the first two terms in the expansion are retained in order to achieve second order accuracy in time. The time derivative of $\boldsymbol{\Phi}$ is converted to a function of $\boldsymbol{h}$ and their space derivatives by making use of the governing equations (Cauchy–Kovalevskaya). The resulting formula of $\boldsymbol{F}$ is

$$\boldsymbol{F} = \Delta t\boldsymbol{\Phi} - \frac{(\Delta t)^2}{2}\frac{\partial \boldsymbol{\Phi}}{\partial \tilde{\boldsymbol{h}}}\cdot\left(\frac{\partial \boldsymbol{\Phi}}{\partial x} + \frac{\partial \boldsymbol{\Psi}}{\partial y}\right), \tag{8}$$

where each term on the right hand side is evaluated at $t=0$. Incidentally, the matrix $\partial\boldsymbol{\Phi}/\partial\tilde{\boldsymbol{h}}$ is computed by using the chain-rule:

$$\frac{\partial \boldsymbol{\Phi}}{\partial \tilde{\boldsymbol{h}}} = \frac{\partial \boldsymbol{\Phi}}{\partial \boldsymbol{h}}\cdot\frac{\partial \boldsymbol{h}}{\partial \tilde{\boldsymbol{h}}}, \tag{9}$$

where the matrix $\partial\boldsymbol{h}/\partial\tilde{\boldsymbol{h}}$ can be computed as the inversion of $\partial\tilde{\boldsymbol{h}}/\partial\boldsymbol{h}$ or by expressing $\boldsymbol{h}$ in terms of $\tilde{\boldsymbol{h}}$.

The formula of $\boldsymbol{F}$ becomes explicit when the distribution of $\boldsymbol{h}$ (or $\tilde{\boldsymbol{h}}$) around cell-edge is specified. The above derivation assumes the smoothness of the solution, and consequently, the resulting scheme is the Lax–Wendroff type.

### 2.5. Kinetic numerical flux

A procedure similar to the derivation of the finite volume Lax–Wendroff method leads to the kinetic expression of Eq. (8) from Eq. (5):

$$\boldsymbol{F} = \int_0^{\Delta t}\int_{R^3} \zeta_x \boldsymbol{\phi} f\,d\zeta_x\,d\zeta_y\,d\zeta_z\,dt, \tag{10}$$

$$f = g - t\frac{\partial g}{\partial \tilde{\boldsymbol{h}}}[\Delta\boldsymbol{\Phi} + \Delta\boldsymbol{\Psi}], \tag{11}$$

where $\Delta\boldsymbol{\Phi}$ and $\Delta\boldsymbol{\Psi}$ correspond to $\partial\boldsymbol{\Phi}/\partial x$ and $\partial\boldsymbol{\Psi}/\partial y$, respectively, and they are given by

$$\begin{pmatrix}\Delta\boldsymbol{\Phi}\\ \Delta\boldsymbol{\Psi}\end{pmatrix} = \int_{R^3}\boldsymbol{\phi}\begin{pmatrix}\zeta_x\frac{\partial g}{\partial x}\\ \zeta_y\frac{\partial g}{\partial y}\end{pmatrix}d\zeta_x\,d\zeta_y\,d\zeta_z. \tag{12}$$

Each term on the right hand side of Eq. (11) is evaluated at $t=0$. The derivatives $\partial g/\partial\tilde{\boldsymbol{h}}$ are computed in the same way as $\partial\boldsymbol{\Phi}/\partial\tilde{\boldsymbol{h}}$ and $\partial g/\partial s$ $(s=x,y)$ are computed as $(\partial g/\partial\boldsymbol{h})\cdot(\partial\boldsymbol{h}/\partial s)$. When the reconstruction of $\boldsymbol{h}$ (or $\tilde{\boldsymbol{h}}$) is smooth, the resulting scheme is the Lax–Wendroff type as before. If the reconstruction is discontinuous at a cell-edge, say $x=0$, $\boldsymbol{h}$ has two limiting values there:

$$\boldsymbol{h}^L = \lim_{x\to 0-}\boldsymbol{h}, \qquad \boldsymbol{h}^R = \lim_{x\to 0+}\boldsymbol{h}. \tag{13}$$

In general, its spatial derivative $\partial\boldsymbol{h}/\partial s$ $(s=x,y)$ also has two limiting values there:

$$\left(\frac{\partial \boldsymbol{h}}{\partial s}\right)^L = \lim_{x\to 0-}\frac{\partial \boldsymbol{h}}{\partial s}, \qquad \left(\frac{\partial \boldsymbol{h}}{\partial s}\right)^R = \lim_{x\to 0+}\frac{\partial \boldsymbol{h}}{\partial s}. \tag{14}$$

The $g$ and $\partial g/\partial s$ $(s=x,y)$ for the reconstruction of the distribution of $\boldsymbol{h}$ with discontinuities at the cell-edge, which will be hereafter denoted by $g_D$ and $(\partial g/\partial s)_D$, respectively, are defined according to the kinetic upstream principle:

$$g_D = \begin{cases} g(\boldsymbol{h}^R,\zeta_x,\zeta_y,\zeta_z) & \zeta_x < 0,\\ g(\boldsymbol{h}^L,\zeta_x,\zeta_y,\zeta_z) & \zeta_x > 0,\end{cases} \tag{15}$$

$$\left(\frac{\partial g}{\partial s}\right)_D = \begin{cases} \frac{\partial g}{\partial s}(\boldsymbol{h}^R, \left(\frac{\partial \boldsymbol{h}}{\partial s}\right)^R, \zeta_x, \zeta_y, \zeta_z) & \zeta_x < 0, \\ \frac{\partial g}{\partial s}(\boldsymbol{h}^L, \left(\frac{\partial \boldsymbol{h}}{\partial s}\right)^R, \zeta_x, \zeta_y, \zeta_z) & \zeta_x > 0. \end{cases} \tag{16}$$

This principle follows from the simple fact that the propagation of information in a gas is brought by the molecular motion; the physically plausible principle yields positive dissipation and vice versa for the nonphysical downstream principle ($\zeta_x \gtrless 0, x \to 0\pm$). KLW in Ref. [20] adopts another approximation of $g$, which was first employed in GKB. Let $\boldsymbol{h}^C$ be the primitive variables computed from $g_D$; $\boldsymbol{h}^C$ are readily obtained from $\boldsymbol{h}$ for $g_D$. Further, let $g_C$ and $(\partial g/\partial \tilde{\boldsymbol{h}})_C$ be the equilibrium distribution function $g$ and its derivatives $\partial g/\partial \tilde{\boldsymbol{h}}$ for $\boldsymbol{h} = \boldsymbol{h}^C$, respectively, i.e.

$$g_C = g(\boldsymbol{h}^C, \zeta_x, \zeta_y, \zeta_z), \tag{17}$$

$$\left(\frac{\partial g}{\partial \tilde{\boldsymbol{h}}}\right)_C = \frac{\partial g}{\partial \tilde{\boldsymbol{h}}}(\boldsymbol{h}^C, \zeta_x, \zeta_y, \zeta_z). \tag{18}$$

Now all the materials necessary for the construction of the scheme are prepared.

Eqs. (11) and (12) are modified as

$$f = (1-\alpha) g_C + \alpha g_D - t\left(\frac{\partial g}{\partial \tilde{\boldsymbol{h}}}\right)_C \cdot \left[(\Delta \boldsymbol{\Phi})_D + (\Delta \boldsymbol{\Psi})_D\right], \tag{19}$$

$$\begin{pmatrix} (\Delta \boldsymbol{\Phi})_D \\ (\Delta \boldsymbol{\Psi})_D \end{pmatrix} = \int_{R^3} \boldsymbol{\phi} \begin{pmatrix} \zeta_x (\frac{\partial g}{\partial x})_D \\ \zeta_y (\frac{\partial g}{\partial y})_D \end{pmatrix} d\zeta_x \, d\zeta_y \, d\zeta_z, \tag{20}$$

where $\alpha$ is a parameter in the range $0 \leqslant \alpha \leqslant 1$ and will be hereafter called the jump indicator. As mentioned previously, the kinetic scheme based on Eqs. (19) and (20) is reduced to the Lax–Wendroff type scheme when the reconstruction of $\boldsymbol{h}$ (or $\tilde{\boldsymbol{h}}$) is smooth; $g_D = g_C$ in this case. It also goes back to EFM if the reconstruction of $\boldsymbol{h}$ (or $\tilde{\boldsymbol{h}}$) is piecewise constant and $\alpha = 1$; $(\partial g/\partial s)_D = 0$ in this case. While $g_D$ generates a lot of numerical dissipation, $g_C$ is less dissipative although it is more dissipative than $g$ generated from a smooth reconstruction. The value of the jump indicator $\alpha$ should be given such that the contribution of $g_D$ becomes dominant around shock waves and vice versa in smooth regions, such as boundary-layers, where the scheme behaves like the Lax–Wendroff type scheme. This scheme can be regarded as a hybrid scheme consisting of two diffusive schemes. Because of the dissipation of $g_C$, a lot of special care is not needed in the determination of $\alpha$. For example, the ad hoc formula

$$\alpha = 1 - \exp\left(-10 \frac{|P^L - P^R|}{P^L + P^R}\right), \tag{21}$$

which is adopted in the present study, works quite satisfactorily; the pressure jump is employed in order to avoid the excessive numerical dissipation generated by $g_D$ inside boundary-layers. If $g_C$ is replaced by $g((\boldsymbol{h}^L + \boldsymbol{h}^R)/2, \ldots)$, which corresponds to the Lax–Wendroff scheme, the resulting hybrid scheme does not work well. The reader can easily confirm it in simple tests, such as the Sod test case. The existence of overlap width is the key for successful hybridization.

The explicit formula of $\boldsymbol{F}$ is readily obtained by carrying out the integration with respect to $\zeta_x$, $\zeta_y$, and $\zeta_z$ (see Appendix A); no numerical integration with respect to the molecular velocity is necessary in the actual numerical computation.

### 2.6. Extension to Navier–Stokes

The extension to the case of the compressible Navier–Stokes equations is usually made by adding the diffusive flux approximated by an appropriate central finite difference formula. This convention is obediently adopted in the extension of KLW. It is also possible to employ the results of Chapman–Enskog expansion. It is, however, not necessary because of the following reason [20]. The leading correction to $g$ in the expansion, say $\mathrm{Kn} f_1$, which yields the diffusive flux of the compressible Navier–Stokes equations, is very small; the Knudsen number Kn is very small or the Reynolds number is very large. Even if the correction is approximated as a discontinuous function like $g$, its dissipation is much smaller than the one generated from $g$. If it is smoothly approximated, the result is the same as the one obtained previously. As for the approximation of the diffusive flux with respect to time, a first order accurate formula (the Euler method) usually suffices owing to its smallness. Nevertheless, second order accuracy is effectively achieved while the time step is larger than Kn. For the extension beyond Navier–Stokes and that to higher order accuracy, we refer the reader to Ref. [27].

### 2.7. Extension to general specific heat

Let $E$ be a parameter describing the internal energy of the gas other than the translational mode. We introduce a marginal function $H(E, T)$ satisfying

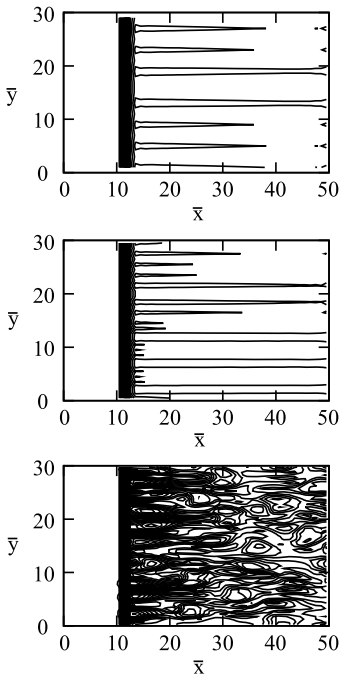


**Fig. 1.** The contours of the nondimensional density (KLW without remedy). Upper: $\Delta y/\Delta x = 2$; middle: $\Delta y/\Delta x = 1$; and lower: $\Delta y/\Delta x = 0.5$. The range is $[0.94 \leqslant \rho/\rho_{up} \leqslant 5.98]$ (73 levels).

$$\int_0^\infty \begin{pmatrix} 1 \\ E \end{pmatrix} H(E,T)\,dE = \begin{pmatrix} 1 \\ B(T) \end{pmatrix}, \tag{22}$$

where $3T/2 + B(T)$ is the total internal energy. The equilibrium function is extended to $gH(E,T)$ together with the replacement of the definition of the weight $\phi_5$ by $\phi_5 = (\zeta_x^2 + \zeta_y^2 + \zeta_z^2)/2 + E$. The integration with respect to $E$ over $(0, +\infty)$ is also introduced. The explicit functional form of $H(E,T)$ is not necessary since only the result of the integration is employed. In all the numerical computations of the present study, the gas is assumed to be diatomic, i.e. $B(T) = T$.

## 3. Diagnosis

The flaws of KLW will be diagnosed in some representative test cases. MUSCL reconstruction with van Leer slope limiter will be employed in all the 2nd order accurate computations. Comparisons will be made with the 2nd order accurate shock-capturing schemes of HLL and AUSM [28–30] families, where the 2nd order accurate RK method will be employed besides MUSCL. Further, the robustness of EFM will be demonstrated together with the assessment of the 1st order accurate schemes of HLL and AUSM families, where the same piecewise constant reconstruction as in Godunov's method and the Euler method (time integration) will be employed.

### 3.1. Simplified odd-even decoupling

Quirk's odd-even decoupling test [1] is well-known as a very useful test for the assessment of the resistance of numerical schemes against shock instabilities. A moving plane normal shock wave is computed on a regular grid system with a slight perturbation in one of the grid lines parallel to the direction of the flow. Because the exact solution is uniform in the whole domain except around the shock wave and no numerical dissipation is generated there in principle, the problem is ideal for the extraction of the nature of test schemes in shock-capturing. A similar test, which is simpler but still keeps the essence, is proposed in Ref. [6], where a stationary plane normal shock wave is computed on a regular grid system. Instead of the perturbation in the grid system, slight random disturbances are inoculated into the initial data (the exact solution, thin shock). We will diagnose the flaws of KLW in this simplified test.

The computational condition is as follows. All the cells are rectangles of the same size $\Delta x \times \Delta y$ and the computational domain, which is denoted by $\Omega$, is $[0 \leqslant x \leqslant 50\Delta x] \times [0 \leqslant y \leqslant 30\Delta x]$. Initially, a standing normal shock wave for the upstream Mach number 6 is located on the line $x = 12\Delta x$ and random disturbances of the relative magnitude of $10^{-6}$ are inoculated into the initial data. The boundary conditions at upstream ($x = 0$) and downstream are fixed and the periodic condition is imposed at the upper boundary and the lower one. Fig. 1 shows the contours of the normalized density $\rho/\rho_{up}$ for the cell aspect ratio $\Delta y/\Delta x = 0.5$, 1, and 2; these results are taken after 10,000 time steps; the time step $\Delta t$

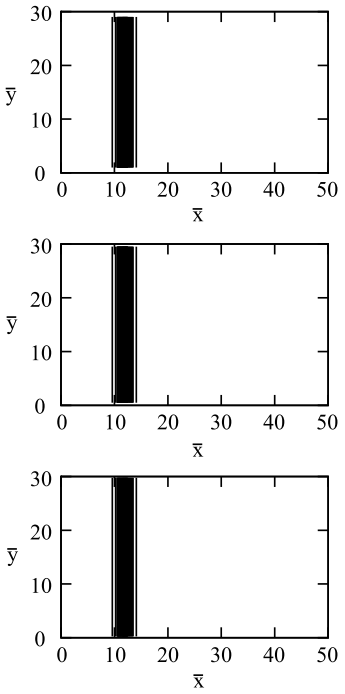


**Fig. 2.** The contours of the nondimensional density (EFM).

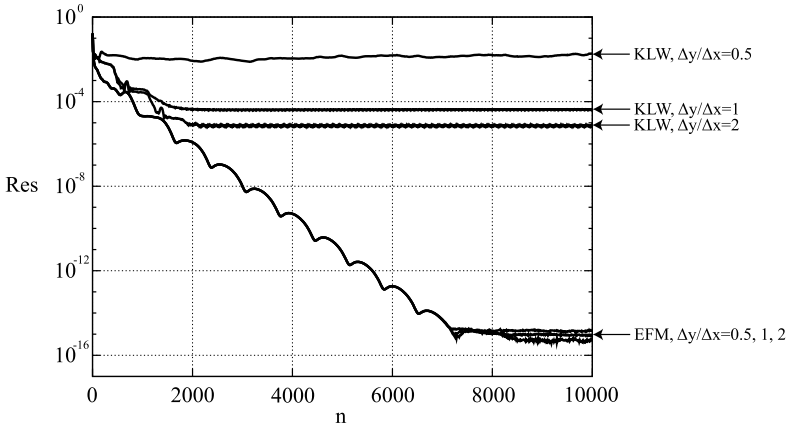


**Fig. 3.** The histories of *Res* (KLW without remedy and EFM) for $\Delta y/\Delta x = 0.5, 1, 2$.

is $0.1\Delta x/\sqrt{2T_{up}}$; $\rho_{up}$ and $T_{up}$ are the density and the temperature at upstream condition, respectively; the normalized coordinates $(\bar{x}, \bar{y}) = (x/\Delta x, y/\Delta x)$ are employed in the figure. KLW exhibits saw-tooth like disturbances for $\Delta y/\Delta x = 1$ and 2 and they grow to the carbuncle phenomenon for $\Delta y/\Delta x = 0.5$. The results of EFM are shown in Fig. 2 for comparison. In contrast to KLW, EFM does not exhibit any appreciable shock anomalies irrespective of the cell aspect ratio. As the magnitude of the disturbances, we measured the residual defined by

$$Res(n) = \frac{1}{S(\Omega)\rho_{up}} \int_{\Omega} \left| \rho\big(x, y, (n+1)\Delta t\big) - \rho(x, y, n\Delta t) \right| dx dy, \tag{23}$$

where $S(\Omega)$ is the area of the computational domain $\Omega$. The histories of *Res* for $\Delta y/\Delta x = 0.5$, 1, and 2 are shown in Fig. 3. The convergence to the steady state is effectively achieved in the computation of EFM, while KLW does not exhibit any signs of it; *Res* oscillates around $2 \times 10^{-2}$, $4 \times 10^{-5}$, and $7 \times 10^{-6}$ for $\Delta y/\Delta x = 0.5$, 1, and 2, respectively. The diagnosis is also carried out for the case where the same shock wave is not aligned with grid lines. The grid system for $\Delta y/\Delta x = 1$ is employed and the shock wave is located along the line $y = (x - 12\Delta x)\tan\theta$ initially. The periodic boundary condition is suitably modified. The density fields for $\tan\theta = 3/5$ ($\theta \sim \pi/6$) and $\tan\theta = 1$ ($\theta = \pi/4$) are shown in Figs. 4 (KLW) and 5 (EFM). In these computations, the inoculation of disturbances into the initial data is not necessary. KLW exhibits the

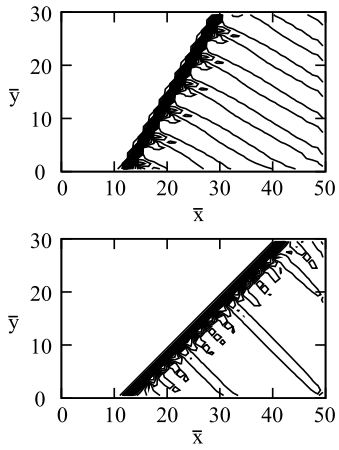


**Fig. 4.** The contours the nondimensional density (KLW without remedy, $\Delta y/\Delta x = 1$). Upper: $\tan\theta = 3/5$ and lower: $\tan\theta = 1$.

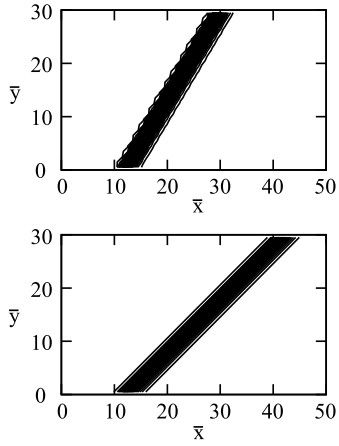


**Fig. 5.** The contours of the nondimensional density (EFM, $\Delta y/\Delta y = 1$). Upper: $\tan\theta = 3/5$ and lower: $\tan\theta = 1$.

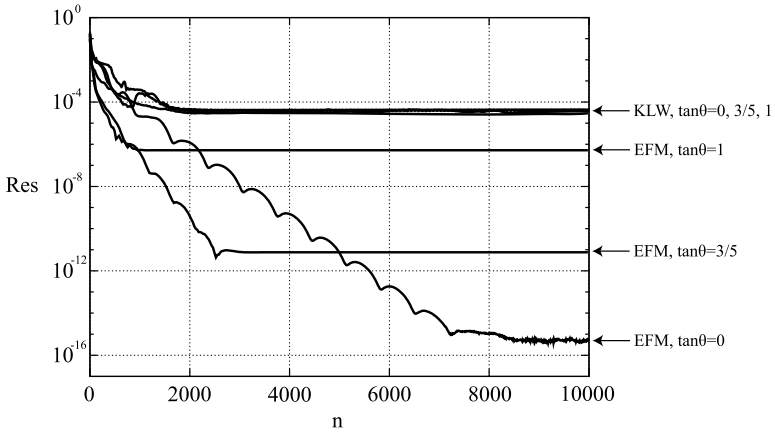


**Fig. 6.** The histories of *Res* (KLW without remedy and EFM) for $\tan\theta = 0, 3/5, 1$ ($\Delta y/\Delta x = 1$).

post-shock oscillations, while no appreciable disturbances are observed in the case of EFM. The histories of *Res* for $\theta = 0$, $\theta \sim \pi/6$, and $\theta = \pi/4$ are shown in Fig. 6. In the case of KLW, *Res* oscillates around $4 \times 10^{-5}$, $4 \times 10^{-5}$, and $3 \times 10^{-5}$ for $\theta = 0$, $\theta \sim \pi/6$, and $\theta = \pi/4$, respectively ($\Delta y/\Delta x = 1$). It should be remarked that even EFM is not free from the post-shock oscillations, although the magnitude of the disturbances is much smaller than that of KLW; *Res* oscillates around $8 \times 10^{-12}$ for $\theta \sim \pi/6$ and $5 \times 10^{-7}$ for $\theta = \pi/4$. On the other hand, the robustness of the 1st order accurate HLLE scheme is not so satisfactory as that of EFM. It does not exhibit any signs of the convergence to the steady state; *Res* oscillates

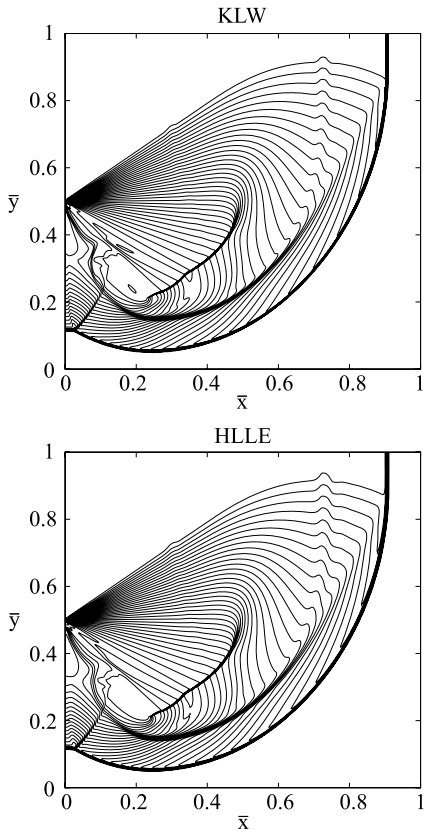


**Fig. 7.** The contours of the nondimensional density in the shock diffraction. The range is $[0.13 \leqslant \rho/\rho_* \leqslant 4.94]$ (38 levels).

around $7 \times 10^{-2}$, $5 \times 10^{-2}$, and $4 \times 10^{-2}$ for $\Delta y/\Delta x = 0.5$, 1, and 2, respectively ($\theta = 0$) and $7 \times 10^{-7}$ and $2 \times 10^{-3}$ for $\theta \sim \pi/6$ and $\theta = \pi/4$, respectively ($\Delta y/\Delta x = 1$). Although HLLE does not exhibit the carbuncle phenomenon in this test, the propagation of vortex-like disturbances is observed in the case of $\theta = 0$. The anomaly of the 1st order accurate HLLE scheme has also been pointed out in Refs. [9,10] and it is contrary to the prediction inferred from the theoretical result in Ref. [6].

### 3.2. Shock diffraction

The diagnosis is carried out in the problem of the diffraction of a plane normal shock wave moving at the Mach number 5.09 (inviscid flow) into a uniform gas at rest ($\rho = \rho_*$, $T = T_*$) over a 90° corner. The computational domain is a square and is divided into $400 \times 400$ square cells of the same size. The corner is located at the midpoint of the left boundary; the inflow boundary condition is imposed at the upper half part and the slip boundary condition is imposed at the lower half part of the left boundary and the top boundary. The time step $\Delta t$ is $0.1\Delta x/\sqrt{2T_*}$. The contours of $\rho/\rho_*$ at $t = 840\Delta t$ are shown in Fig. 7 (KLW and the 2nd order accurate HLLE), where the spatial coordinates normalized by the length of the side of the computational domain, $(\bar{x}, \bar{y})$, are employed. The result of KLW and that of the 2nd order accurate HLLE scheme are nearly indentical and the expansion shock and the post-shock oscillations, which are mentioned in the literature as the typical pathologies in this case, are not observed. This is in contrast to the case of the 2nd order accurate AUSM$^+$ and HLLC, which exhibit small but appreciable post-shock oscillations (no figure).

### 3.3. Hypersonic inviscid flow past a cylinder

The diagnosis is carried out in the problem of a uniform hypersonic inviscid flow past a cylinder. The setting of the problem is as follow. The upstream flow is in the $x$ direction and the Mach number is 6, the axis of the cylinder is located at the origin $x = y = 0$, and the computational domain $\Omega$ is symmetric about $x$ axis, i.e. $\Omega = \Omega_{y>0} + \Omega_{y<0}$ and $\Omega_{y<0}$ is the mirror image of $\Omega_{y>0}$. Because of the symmetry of the problem, *Asy* defined by

$$Asy = \frac{1}{S(\Omega_{y>0})\rho_{up}} \int_{\Omega_{y>0}} \left|\rho(x, y, t) - \rho(x, -y, t)\right| dx\,dy, \tag{24}$$

**Table 1**
The residual *Res* and asymmetry *Asy* for various cases of resolutions. KLW (without remedy, Mesh-A). NaN means that a floating-point exception occurred during the computation.

| $n_\eta$ | $n_\xi$ | | | | |
|---|---|---|---|---|---|
| | 15 | 30 | 60 | 120 | 240 |
| *Res* | | | | | |
| 40 | 7E−16 | 8E−16 | 1E−15 | NaN | NaN |
| 80 | 9E−16 | 3E−14 | 1E−15 | 4E−05 | 2E−15 |
| 160 | 1E−03 | 8E−05 | 1E−15 | 2E−13 | 1E−15 |
| 320 | 8E−03 | 5E−03 | 1E−06 | 9E−06 | 9E−08 |
| 480 | 8E−03 | 7E−03 | 2E−04 | 5E−07 | 1E−07 |
| *Asy* | | | | | |
| 40 | 9E−15 | 1E−14 | 2E−14 | NaN | NaN |
| 80 | 1E−14 | 7E−03 | 2E−14 | 1E−14 | 2E−14 |
| 160 | 3E−02 | 8E−09 | 1E−14 | 1E−14 | 2E−14 |
| 320 | 2E−01 | 8E−02 | 5E−10 | 2E−03 | 3E−07 |
| 480 | 4E−01 | 1E−01 | 5E−03 | 3E−06 | 1E−06 |

should be zero without shock instabilities. The numerical solution is always subject to the influence of round-off errors, which are said to trigger the carbuncle phenomenon. Since they are not symmetric even in the present setting, it is considered that the carbuncle phenomenon is accompanied by the symmetry breaking. For this reason we employ *Asy* as an index of the pathology. Shock instabilities are sensitive to mesh system and two mesh systems are prepared in the diagnosis. One mesh system, Mesh-A, is defined by

$$\begin{aligned}
&\bar{x} = (1-\xi)(a_1\cosh\eta - a_2) - \xi\cos\eta,\\
&\bar{y} = a_3(1-\xi)\sinh\eta + \xi\sin\eta,\\
&a_1 = 2.45, \qquad a_2 = 4.736, \qquad a_3 = 3.185,\\
&\frac{1}{2} \leqslant \xi \leqslant 1, \qquad -\frac{2\pi}{5} \leqslant \eta \leqslant \frac{2\pi}{5},
\end{aligned} \tag{25}$$

where the spatial coordinates are normalized by the radius of the cylinder and the interval for $\xi$ ($\eta$) is divided into $n_\xi$ ($n_\eta$) uniform sections. These grid lines constitute the cell-edges. The values of the parameters $a_i$ ($i = 1, 2, 3$) are chosen in such a way that the grid lines for $\xi = \text{Const.}$ around the shock wave align with it very well (the alignment is not perfect). The other mesh system, Mesh-B, is the cylindrical one defined by

$$\begin{aligned}
&\bar{x} = -(3.8 - 2.8\xi)\cos\eta,\\
&\bar{y} = (3.8 - 2.8\xi)\sin\eta.
\end{aligned} \tag{26}$$

The intervals for $\xi$ and $\eta$ are the same as those in Mesh-A and they are uniformly divided as before. The residual defined by Eq. (23) will be employed as a measure of the magnitude of time-dependent disturbances; the definitions of $\rho_{up}$ and $\Omega$ change but no confusion will take place. The time step $\Delta t$ employed in all the following computations is $0.1\Delta_{min}/\sqrt{2T_{up}}$, where $\Delta_{min}$ stands for the minimum cell-width.

The numerical solution either converges to the steady state effectively or oscillates around a certain state as time passes. The convergence to the steady state, i.e. the vanishment of *Res*, does not necessarily mean the soundness of the numerical computation. As will be seen later, a number of wrinkles can appear behind the shock wave even if *Res* effectively vanishes; this pathology will be hereafter called the post-shock wrinkles. It should also be mentioned that the vanishment of *Asy* does not exclude the case of symmetric disturbances. The data of *Asy* and *Res* for various resolutions (KLW) are shown in Table 1 (Mesh-A) and Table 2 (Mesh-B). They were measured after sufficiently long time had passed, i.e. $t = 50/\sqrt{2T_{up}}$ (the radius of the cylinder is taken as unity). For comparison, the results of AUSM$^+$, AUSM$^+$-up, SLAU, HLLE, and HLLC (2nd order accuracy, Mesh-A) are shown in Tables 3–7. These tables indicate that KLW and the 2nd order accurate shock-capturing schemes with advanced Riemann solvers are subject to some kind of shock instabilities. The same conclusion is drawn from the results for Mesh-B. The density fields obtained by these 2nd order accurate schemes for Mesh-A and $(n_\xi, n_\eta) = (120, 320)$ are shown in Fig. 8. It is seen that all the schemes exhibit shock anomalies, i.e. the carbuncle phenomenon, the post-shock oscillations, and the post-shock wrinkles. Incidentally, it should be highlighted that EFM exhibits no shock anomalies (*Res* and *Asy* are effectively zero) irrespective of mesh system and resolution. The density field obtained by EFM for Mesh-B and $(n_\xi, n_\eta) = (120, 320)$ is shown in Fig. 9 together with those obtained by the 1st order accurate AUSM and HLL schemes. A 1st order accurate scheme is generally considered to be more robust than the corresponding 2nd order accurate one and some improvements in the resistance to shock instabilities are expected. The 1st order accurate AUSM$^+$-up, SLAU, and HLLC schemes still exhibit the carbuncle phenomenon. Although AUSM$^+$ and HLLE effectively achieve the steady state and *Asy* for HLLE is also effectively zero in this case (*Asy* for AUSM$^+$ is $2 \times 10^{-4}$), they still produce distortion just behind the shock wave. Unlike in the case of EFM, *Asy* and *Res* do not vanish in all the cases of mesh system.

**Table 2**
KLW (without remedy, Mesh-B).

| $n_\eta$ | $n_\xi$ | | | | |
|---|---|---|---|---|---|
| | 15 | 30 | 60 | 120 | 240 |
| *Res* | | | | | |
| 40 | 1E−15 | 2E−15 | 3E−15 | 3E−04 | 5E−04 |
| 80 | 6E−03 | 2E−03 | 2E−04 | 7E−06 | 2E−04 |
| 160 | 2E−02 | 9E−03 | 2E−03 | 5E−07 | 8E−06 |
| 320 | 1E−02 | 1E−02 | 5E−03 | 2E−03 | 5E−05 |
| 480 | 1E−02 | 1E−02 | 6E−03 | 2E−03 | 4E−04 |
| *Asy* | | | | | |
| 40 | 2E−14 | 1E−14 | 2E−14 | 3E−14 | 8E−14 |
| 80 | 2E−01 | 5E−12 | 3E−05 | 2E−14 | 1E−03 |
| 160 | 3E−01 | 6E−02 | 3E−02 | 2E−14 | 1E−04 |
| 320 | 9E−01 | 3E−01 | 6E−02 | 1E−02 | 3E−05 |
| 480 | 4E−01 | 3E−01 | 8E−02 | 2E−02 | 4E−04 |

**Table 3**
AUSM+ (2nd order, Mesh-A).

| $n_\eta$ | $n_\xi$ | | | | |
|---|---|---|---|---|---|
| | 15 | 30 | 60 | 120 | 240 |
| *Res* | | | | | |
| 40 | 7E−16 | 2E−03 | 6E−04 | NaN | NaN |
| 80 | 8E−16 | 3E−03 | 6E−04 | 2E−04 | 4E−04 |
| 160 | 5E−04 | 2E−03 | 6E−04 | 2E−04 | 4E−04 |
| 320 | 2E−03 | 1E−03 | 5E−04 | 2E−03 | 5E−04 |
| 480 | 2E−03 | 3E−03 | 4E−04 | 2E−03 | 5E−04 |
| *Asy* | | | | | |
| 40 | 3E−07 | 6E−07 | 2E−03 | NaN | NaN |
| 80 | 1E−14 | 8E−08 | 8E−04 | 2E−03 | 3E−03 |
| 160 | 1E−02 | 4E−08 | 1E−03 | 3E−03 | 3E−03 |
| 320 | 6E−02 | 2E−09 | 4E−04 | 2E−02 | 6E−03 |
| 480 | 7E−02 | 3E−02 | 6E−03 | 3E−02 | 6E−03 |

**Table 4**
AUSM+-up (2nd order, Mesh-A).

| $n_\eta$ | $n_\xi$ | | | | |
|---|---|---|---|---|---|
| | 15 | 30 | 60 | 120 | 240 |
| *Res* | | | | | |
| 40 | 2E−13 | 4E−03 | 1E−03 | NaN | NaN |
| 80 | 3E−03 | 5E−03 | 1E−03 | 9E−04 | 8E−04 |
| 160 | 3E−03 | 7E−03 | 2E−03 | 1E−03 | 8E−04 |
| 320 | 3E−03 | 6E−03 | 1E−03 | 1E−03 | 2E−03 |
| 480 | 2E−03 | 4E−03 | 2E−03 | 1E−03 | 3E−03 |
| *Asy* | | | | | |
| 40 | 8E−15 | 2E−14 | 1E−14 | NaN | NaN |
| 80 | 5E−02 | 6E−06 | 1E−14 | 6E−03 | 5E−03 |
| 160 | 8E−02 | 2E−13 | 9E−15 | 1E−02 | 5E−03 |
| 320 | 1E−01 | 4E−04 | 2E−14 | 4E−02 | 1E−02 |
| 480 | 9E−02 | 8E−04 | 3E−02 | 2E−02 | 9E−03 |

### 3.4. Contact discontinuity and boundary-layer

Needless to say, numerical dissipation is the key ingredient of shock-capturing schemes. Excessive numerical dissipation, however, brings not only the robustness but also the dullness. Since the capability of KLW in shock capturing is clarified in Sections 3.1–3.3, we assess here the capability of KLW in contact-discontinuity capturing and boundary-layer capturing. Fig. 10 shows the results of KLW and 2nd order accurate HLLE and HLLC schemes for the stationary contact discontinuity with the density ratio $\rho_L/\rho_R = 10$, where the subscripts $L$ and $R$ stand for the left state and the right one, respectively. A uniform mesh system is employed in the computation and the unit length in the space coordinate $\bar{x}$ corresponds to the cell-width $\Delta x$. The capability of sharply capturing contact discontinuities is often mentioned as a noteworthy feature of HLLC; "C" of HLLC stands for contact discontinuity. It indeed captures the stationary discontinuity without inner point. In contrast, both KLW and HLLE yield smeared profiles; the latter result is more diffusive than the former one. The superiority

**Table 5**
SLAU (2nd order, Mesh-A).

| $n_\eta$ | $n_\xi$ | | | | |
|---|---|---|---|---|---|
| | 15 | 30 | 60 | 120 | 240 |
| *Res* | | | | | |
| 40 | 7E−16 | 1E−03 | 3E−03 | 2E−03 | NaN |
| 80 | 6E−15 | 1E−03 | 2E−03 | 2E−03 | 1E−03 |
| 160 | 4E−03 | 1E−03 | 2E−03 | 3E−03 | 1E−03 |
| 320 | 3E−03 | 6E−04 | 2E−03 | 3E−03 | 1E−03 |
| 480 | 2E−03 | 6E−04 | 1E−03 | 1E−03 | 1E−03 |
| *Asy* | | | | | |
| 40 | 1E−14 | 1E−14 | 6E−10 | 4E−13 | NaN |
| 80 | 1E−14 | 8E−15 | 1E−14 | 4E−13 | 1E−02 |
| 160 | 1E−01 | 2E−14 | 9E−03 | 2E−02 | 8E−03 |
| 320 | 1E−01 | 1E−13 | 1E−02 | 8E−03 | 1E−02 |
| 480 | 2E−01 | 1E−03 | 2E−02 | 2E−02 | 1E−02 |

**Table 6**
HLLE (2nd order, Mesh-A).

| $n_\eta$ | $n_\xi$ | | | | |
|---|---|---|---|---|---|
| | 15 | 30 | 60 | 120 | 240 |
| *Res* | | | | | |
| 40 | 1E−14 | 6E−16 | 1E−03 | 7E−04 | NaN |
| 80 | 1E−15 | 8E−16 | 4E−04 | 3E−04 | 4E−04 |
| 160 | 7E−16 | 3E−05 | 2E−04 | 1E−15 | 3E−04 |
| 320 | 3E−04 | 9E−16 | 1E−03 | 2E−15 | 5E−04 |
| 480 | 2E−03 | 5E−06 | 9E−04 | 7E−04 | 7E−04 |
| *Asy* | | | | | |
| 40 | 6E−15 | 9E−15 | 6E−03 | 8E−13 | NaN |
| 80 | 7E−15 | 8E−15 | 1E−13 | 3E−14 | 2E−14 |
| 160 | 1E−14 | 9E−15 | 2E−13 | 2E−14 | 5E−04 |
| 320 | 1E−02 | 1E−14 | 4E−05 | 1E−14 | 6E−03 |
| 480 | 4E−02 | 3E−14 | 9E−14 | 4E−14 | 8E−03 |

**Table 7**
HLLC (2nd order, Mesh-A).

| $n_\eta$ | $n_\xi$ | | | | |
|---|---|---|---|---|---|
| | 15 | 30 | 60 | 120 | 240 |
| *Res* | | | | | |
| 40 | 3E−12 | 8E−05 | 5E−05 | 9E−04 | 3E−04 |
| 80 | 6E−06 | 6E−04 | 1E−03 | 2E−04 | 1E−04 |
| 160 | 2E−03 | 2E−03 | 2E−03 | 4E−04 | 2E−04 |
| 320 | 2E−03 | 2E−03 | 2E−03 | 2E−04 | 3E−04 |
| 480 | 2E−03 | 5E−03 | 2E−03 | 8E−04 | 1E−03 |
| *Asy* | | | | | |
| 40 | 9E−02 | 1E−14 | 1E−14 | 5E−03 | 2E−11 |
| 80 | 3E−02 | 2E−14 | 2E−14 | 2E−11 | 6E−03 |
| 160 | 5E−02 | 3E−02 | 2E−05 | 1E−09 | 6E−06 |
| 320 | 9E−02 | 1E−02 | 4E−14 | 2E−02 | 2E−03 |
| 480 | 9E−02 | 2E−02 | 8E−03 | 3E−02 | 3E−03 |

of HLLC over KLW is confirmed only in this special case, however. When a thin stationary contact discontinuity without structure is employed as the initial data, HLLC can keep it as it is. When the initial data has structure, however, the result of HLLC becomes as diffusive as that of KLW (no figure). The same observation is made in the case of a moving contact discontinuity. Fig. 11 shows the results for the same contact discontinuity moving in the $\bar{x}$ direction with the speed $0.01\sqrt{2T_R}$; the initial data is a thin contact discontinuity without structure. Shock-capturing schemes are not equipped with any mechanisms which sharpen contact discontinuities. This incapability is not, however, serious from the practical point of view; the solution of Euler equations is merely the limit of that of Navier–Stokes equations, which is always accompanied by the diffusion. Incidentally, the time step $\Delta t$ employed in the above computations is $0.1\Delta x/\sqrt{2T_R}$.

The superiority of HLLC over HLLE is also mentioned in connection with boundary-layer capturing. The results of Blasius boundary-layer function $F(\eta)$ obtained by KLW, EFM, and the second order accurate HLLE and HLLC schemes are compared

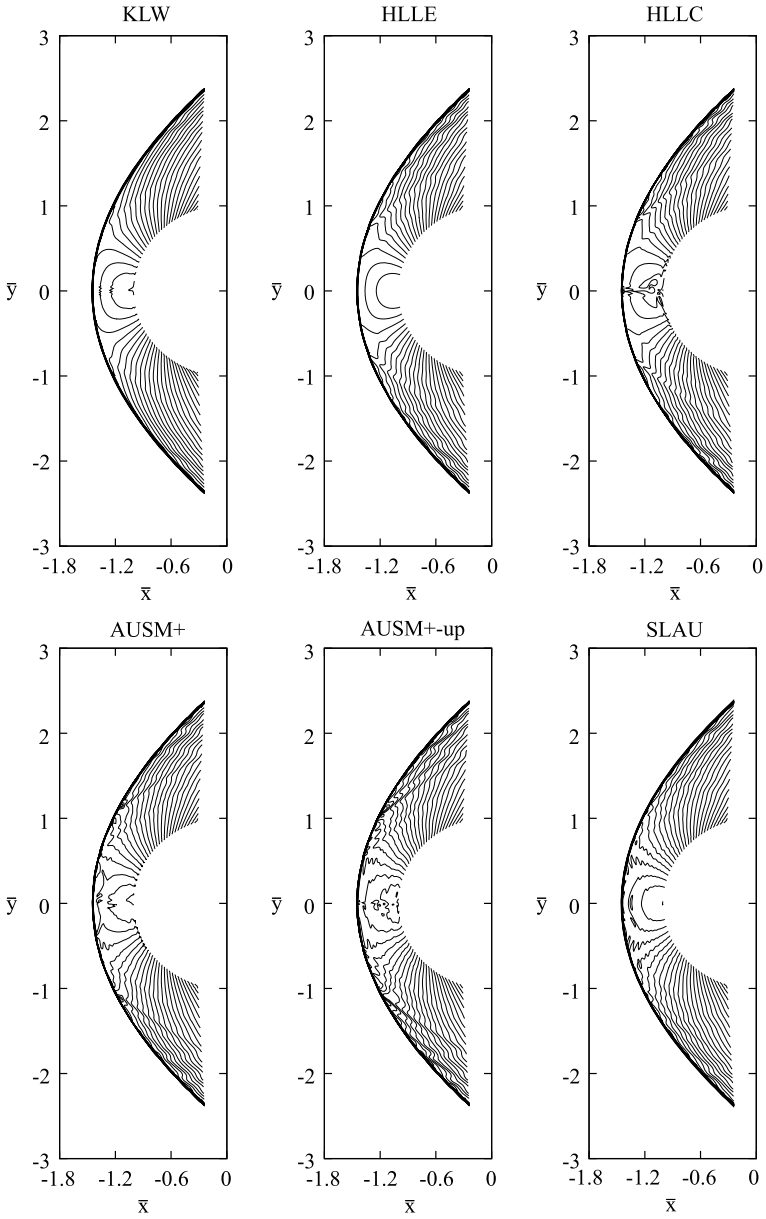


**Fig. 8.** Comparison of density fields for different 2nd order accurate schemes. Mesh-A and $(n_\xi, n_\eta) = (120, 320)$. The range of the isolines is $[1.05 \leqslant \rho/\rho_{up} \leqslant 5.7]$ (32 levels).

in Fig. 12. The results of KLW and HLLC are nearly identical. The results of EFM are very poor even for the four times finer resolution. The superiority of KLW over HLLE is also confirmed in this test.

## 4. Remedy

As seen in the previous section, KLW is not so robust as EFM. One of the reasons is considered to be its insufficient transformation into EFM around shock waves. In this section we will propose a slight modification of the preprocessing to promote the transformation.

### 4.1. New preprocessing

Let us consider for simplicity the case of a Cartesian grid system in 2D. The grid lines are expressed as $x = x_{i+1/2}$ and $y = y_{j+1/2}$ $(i = 0, 1, 2, 3, \ldots,\ j = 0, 1, 2, 3, \ldots)$ and the cell $(i, j)$ is defined by $[x_{i-1/2} < x < x_{x+1/2}] \times [y_{j-1/2} < y < y_{j+1/2}]$. The numerical solution is evaluated at each cell-center point $(x, y) = (x_i, y_j) = ((x_{i-1/2} + x_{i+1/2})/2, (y_{j-1/2} + y_{j+1/2})/2)$.

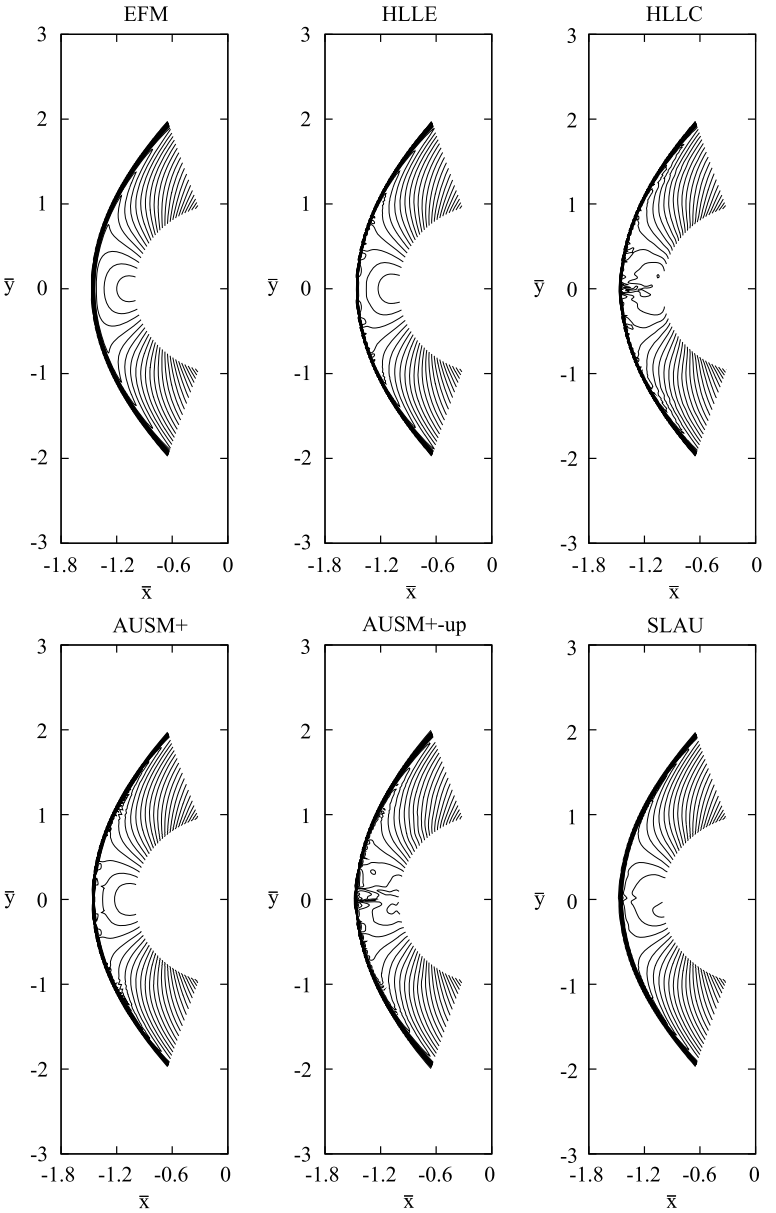


**Fig. 9.** Comparison of density fields for different 1st order accurate schemes. Mesh-B and $(n_\xi, n_\eta) = (120, 320)$.

From these data, the slopes $\partial h_j/\partial x$ and $\partial h_j/\partial y$ and the limiting values of $h_k$ at cell-edges are computed by using an appropriate method for preprocessing, such as MUSCL. The value of the jump indicator $\alpha$ at each cell-edge is computed from the pressure jump there according to Eq. (21). In the original KLW code, these data are immediately supplied to the subroutine which computes the numerical flux. In the new preprocessing, they are recomputed. For ease of explanation we define two sets of pairs of indices $\#_{i+1/2,j}$ and $\#_{i,j+1/2}$:

$$\#_{i+1/2,j} = \big\{(i+1/2+m,\, j), m = -1, 0, 1\big\} \cup \big\{(i,\, j \pm 1/2), (i+1,\, j \pm 1/2)\big\},$$
$$\#_{i,j+1/2} = \big\{(i,\, j+1/2+m), m = -1, 0, 1\big\} \cup \big\{(i \pm 1/2,\, j), (i \pm 1/2,\, j+1)\big\}.$$

The procedure of the recomputation is as follows.

(i) Compute $\beta_{i+1/2,j}$ and $\beta_{i,j+1/2}$ according to

$$\beta_{i+1/2,j} = \max_{(l,m)\in\#_{i+1/2,j}} \{\alpha_{l,m}\}, \qquad \beta_{i,j+1/2} = \max_{(l,m)\in\#_{i,j+1/2}} \{\alpha_{l,m}\},$$

where $\alpha_{l,m}$ stands for the jump indicator $\alpha$ at the cell-edge $(x_l, y_m)$.

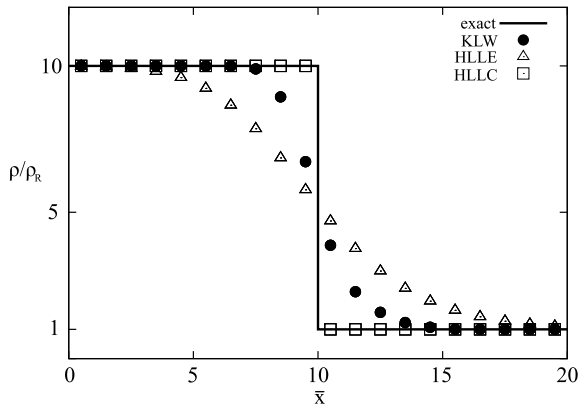


**Fig. 10.** Stationary contact discontinuity.

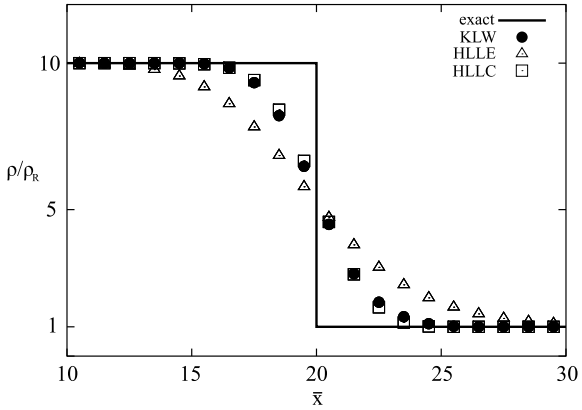


**Fig. 11.** Moving contact discontinuity.

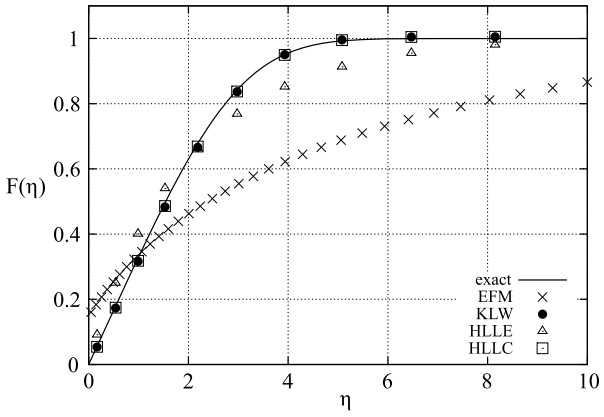


**Fig. 12.** Blasius flow.

(ii) Suppress the magnitudes of the slopes $\partial h_k/\partial s$ $(s = x, y)$ in the cell $(i, j)$ using the values of $\beta_{i\pm1/2,j}$ and $\beta_{i,j\pm1/2}$, which are computed in step (i). Several ad hoc methods are considered for the suppression. For example,

$$\begin{pmatrix} \frac{\partial h_k}{\partial x} \\ \frac{\partial h_k}{\partial y} \end{pmatrix} \rightarrow \begin{pmatrix} \left(1 - \frac{\beta_{i+1/2,j}+\beta_{i-1/2,j}}{2}\right)\frac{\partial h_k}{\partial x} \\ \left(1 - \frac{\beta_{i,j+1/2}+\beta_{i,j-1/2}}{2}\right)\frac{\partial h_k}{\partial y} \end{pmatrix}, \tag{27}$$

$$\begin{pmatrix} \frac{\partial h_k}{\partial x} \\ \frac{\partial h_k}{\partial y} \end{pmatrix} \rightarrow \begin{pmatrix} \left(1 - \frac{\beta_{i,j+1/2}+\beta_{i,j-1/2}}{2}\right)\frac{\partial h_k}{\partial x} \\ \left(1 - \frac{\beta_{i+1/2,j}+\beta_{i-1/2,j}}{2}\right)\frac{\partial h_k}{\partial y} \end{pmatrix}, \tag{28}$$

and so on.

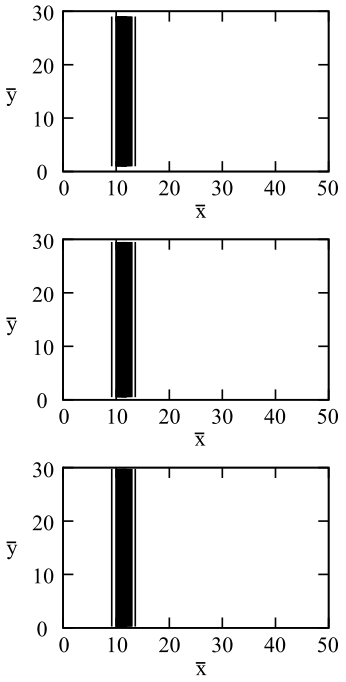


**Fig. 13.** The contours of the nondimensional density (KLWR). Upper: $\Delta y/\Delta x = 2$; middle: $\Delta y/\Delta x = 1$; lower: $\Delta y/\Delta x = 0.5$.

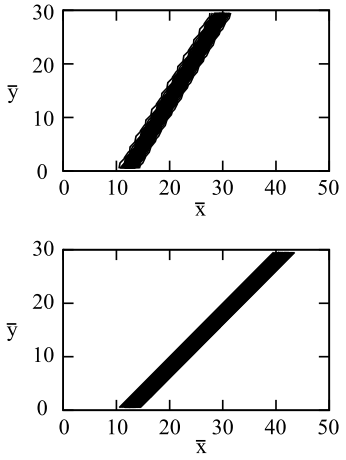


**Fig. 14.** The contour plot of the density field (KLWR, $\Delta y/\Delta x = 1$). Upper: $\tan\theta = 3/5$ and lower: $\tan\theta = 1$.

(iii) Compute the limiting values of $h_k$ at the midpoint of each cell-edge using the modified values of the slopes in the neighboring cells.
(iv) Replace $\alpha_{i,j+1/2}$ and $\alpha_{i+1/2,j}$ by $\beta_{i,j+1/2}$ and $\beta_{i+1/2,j}$, respectively.

The main point of the above modification is to smoothly enhance the transformation of KLW into EFM around shock waves. The sudden transformation causes the occurrence of disturbances and should be avoided. Unless otherwise stated, Eq. (27) will be employed in the computations of the present study. Hereafter we will call KLW with the above remedy KLWR.

### 4.2. Confirmation of efficacy

We present the results of KLWR in the problems of Section 3 where KLW exhibits shock anomalies. Figs. 13 and 14 show the contours of the nondimensional density in the problem of Section 3.1 (simplified odd-even decoupling). KLWR does not produce any appreciable disturbances and captures the shock wave more sharply than EFM does. Fig. 15 shows the histories of the residual *Res*. In the case of $\theta = 0$, the occurrence of shock instabilities is completely suppressed and the convergence

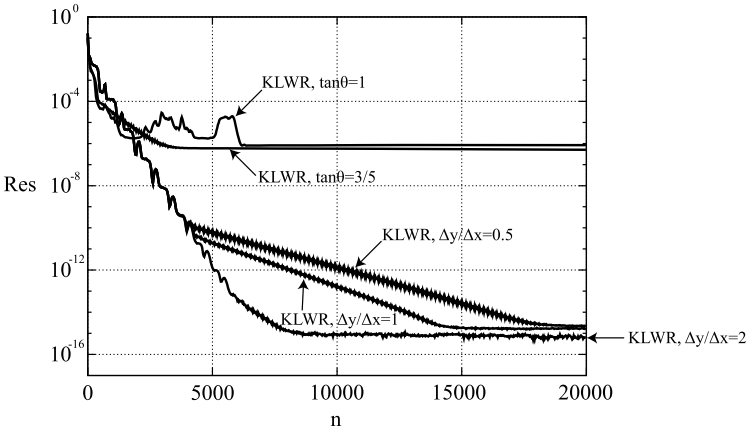


**Fig. 15.** The histories of *Res* (KLWR).

to the steady state is achieved irrespective of the cell aspect ratio. When the grid alignment with the shock wave is poor, the convergence is not achieved even after the remedy, which is expected from the result of EFM. *Res* is kept around $6 \times 10^{-7}$ and $8 \times 10^{-7}$ for $\theta \sim \pi/6$ and $\theta = \pi/4$, respectively; the magnitude of the disturbances reduces to $2 \sim 3\%$ of the value before the remedy. The remedy also works quite satisfactorily in the problem of Section 3.3 (a hypersonic inviscid flow past a cylinder); *Asy* effectively vanishes for all the cases in Tables 1 and 2 and *Res* is also effectively zero except for the case of Mesh-B and $(n_\xi, n_\eta) = (30, 480)$, $(60, 480)$, and $(240, 80)$, where *Res* is less than $2 \times 10^{-7}$. Incidentally, *Asy* and *Res* are effectively zero irrespective of mesh system and resolution if the slopes are suppressed according to Eq. (28). The density fields for $(n_\xi, n_\eta) = (120, 320)$, $(240, 320)$, $(240, 480)$ (Mesh-A and Mesh-B) are shown in Fig. 16. These six density fields are nearly identical and shock anomalies are not seen there; the difference between Eqs. (27) and (28) is invisible in the figure. A slight increase in the thickness of the numerically captured shock wave (from one inner point to three ones) is observed as the side-effect of the remedy, see Fig. 17. If the slopes $\partial h_i/\partial\xi$ are not suppressed (the slopes $\partial h_i/\partial\eta$ are suppressed as before), the shock wave is captured more sharply (one inner point) but shock anomalies are not suppressed completely; a number of wrinkles appear behind the shock wave (no figure).

## 5. Hypersonic viscous flow past a cylinder

The ultimate goal located beyond the present study is the establishment of reliable, efficient, and simple hypersonic viscous flow solvers. In this section we will examine the performance of KLWR in the problem of a hypersonic viscous flow past a cylinder in order to assess the distance to the destination.

The flow configuration is the same as that in the inviscid case (Section 3.3). The gas-dynamic parameters are taken from Ref. [10], where the results of various advanced shock-capturing schemes are presented; the upstream Mach number is 8.1, the Reynolds number based on the radius of the cylinder and the upstream condition is $1.3 \times 10^5$, the temperature dependence of the viscosity is taken into account by using the Sutherland formula, the Prandtl number is 0.72, the nonslip boundary condition is employed at the cylinder surface, the cylinder is at rest, and its surface temperature is maintained at $4.7T_{up}$. In order to resolve the boundary-layer, a non-uniform grid for $\xi$ is introduced in Mesh-A and Mesh-B:

$$\xi = \frac{81 - 41\exp(-\omega)}{80} \quad 0 \leqslant \omega \leqslant \ln(41), \tag{29}$$

where the interval for the parameter $\omega$ is uniformly divided. Recall that Mesh-A is designed for the case of the inviscid flow of the upstream Mach number 6. The grid alignment of Mesh-A with the shock wave in the present case is not so fine as in the previous case. The grid alignment of Mesh-B is still poor. In all the following viscous computations the time step $\Delta t$ is $0.1\Delta_{\min}/\sqrt{2T_{up}}$. The density fields for $(n_\xi, n_\eta) = (120, 160)$, $(180, 240)$, $(240, 320)$ (Mesh-A and Mesh-B) are depicted in Fig. 18. The computations for these six cases yield nearly identical results and shock anomalies are not seen; *Asy* and *Res* effectively vanish irrespective of mesh system and resolution. When the slopes are suppressed according to Eq. (28), these values are effectively zero except for Mesh-B and $(n_\xi, n_\eta) = (120, 160)$ and $(240, 320)$, where *Res* is less than $2 \times 10^{-8}$ and *Asy* is effectively zero; the difference between Eqs. (27) and (28) is invisible in the figure. Incidentally, $Res \sim 10^{-4}$ and $Asy \sim 10^{-3}$ for KLW without the remedy. The distributions of the nondimensional temperature $T/T_{up}$ along $y = 0$ in the boundary-layer for these six cases are compared in Fig. 19. They are nearly identical. The distribution of the nondimensional heat flux $\bar{q}$ (the unit is $\sqrt{2}\hat{\rho}_{up}(R\hat{T}_{up})^{3/2}$, where $\hat{\rho}_{up}$ and $\hat{T}_{up}$ are dimensional density and temperature of the gas at upstream condition and $R$ is the gas constant per unit mass) along the cylinder surface are shown in Fig. 20 as a function of the angle $\chi$ measured from the stagnation point; the position of the cylinder surface is $(x, y) = (r\cos(\pi - \chi), r\sin(\pi - \chi))$. These results are also nearly mesh independent, although small pimple-like variation is observed around $\chi = 0$ in some cases. The value of $\bar{q}$ at the stagnation point ($\chi = 0$) is in good agreement with $\bar{q} = 2.46$, which is predicted by the theory in Ref. [31].

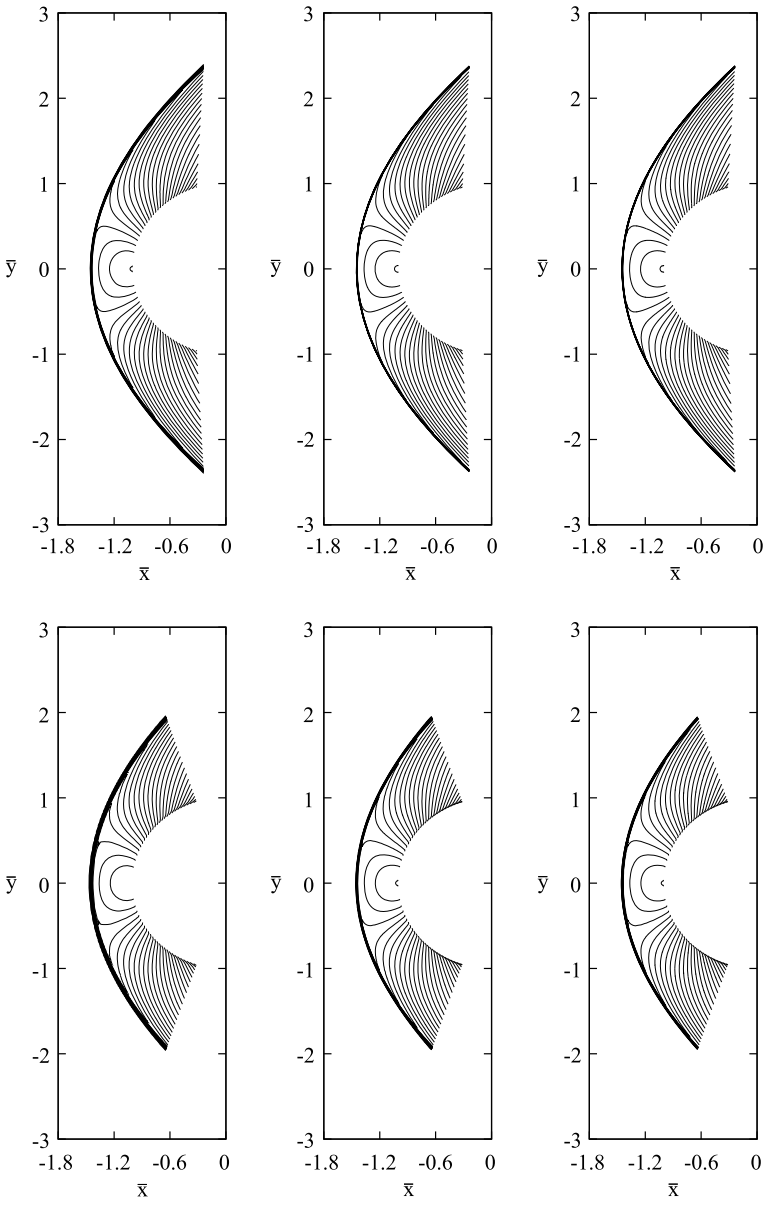


**Fig. 16.** The density fields (KLWR) in Mach 6 inviscid flow past a cylinder. Upper: Mesh-A and lower: Mesh-B. Left: $(n_\xi, n_\eta) = (120, 320)$; middle: $(n_\xi, n_\eta) = (240, 320)$; and right: $(n_\xi, n_\eta) = (240, 480)$. The range of isolines is the same as in Figs. 8 and 9.

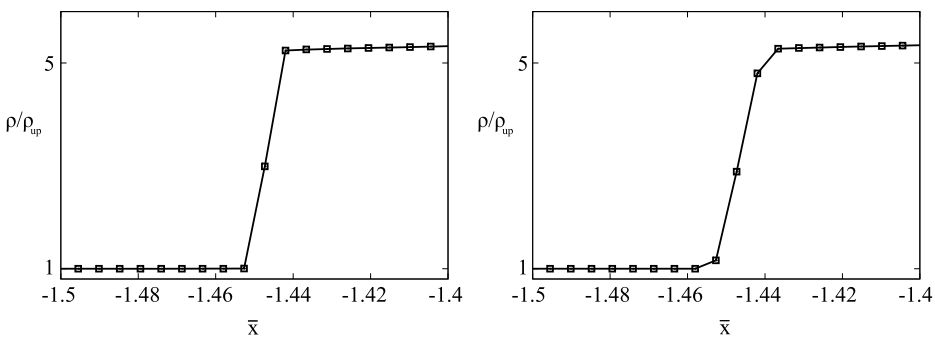


**Fig. 17.** The density distribution along $y = 0$. Left KLW and right KLWR.

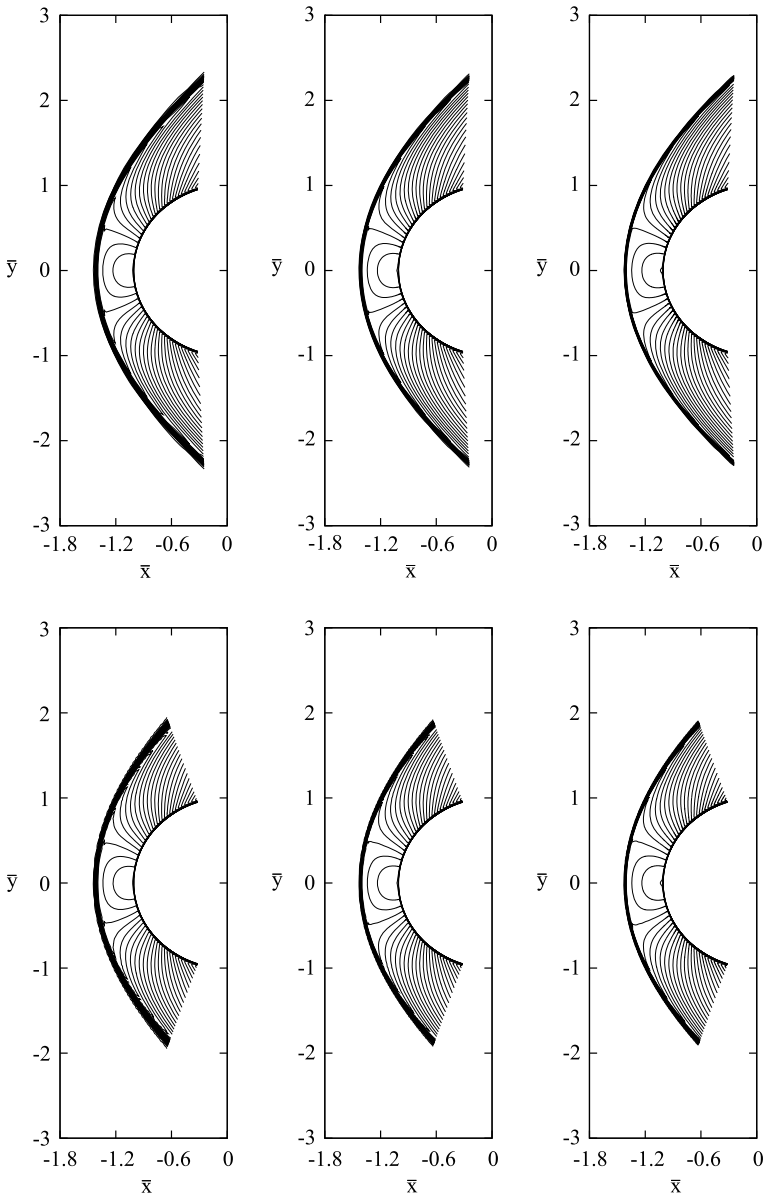


**Fig. 18.** Comparison of density fields in Mach 8.1 viscous flow past a cylinder (KLWR). Upper: Mesh-A and lower: Mesh-B. Left: $(n_\xi, n_\eta) = (120, 160)$; middle: $(n_\xi, n_\eta) = (180, 240)$; and right: $(n_\xi, n_\eta) = (240, 320)$. The range of the isolines is $[1.05 \leqslant \rho/\rho_{up} \leqslant 6.9]$ (40 levels).

From the above results, it is concluded that the present remedy makes KLW effectively free from shock instabilities in the viscous case as well. Incidentally, the 2nd order accurate HLL and AUSM schemes exhibit shock anomalies (no figure). The computation of the hybrid scheme of HLLE and HLLC with the same remedy has also been carried out; the two numerical fluxes are blended and the slopes are suppressed in the same way as in the case of KLWR. The results for the above six cases are depicted in Fig. 21. Although the results are improved and the steady state is established in all the cases owing to the remedy, distortion is clearly observed (Mesh-B) and wrinkles become more appreciable as the resolution increases (Mesh-A). This is not surprising from the fact that the 1st order accurate HLLE is less robust than EFM (Section 3.1 and Fig. 9).

The computational efficiency of KLWR (or KLW) is nearly identical to that of the 2nd order accurate HLLE (and those of other 2nd order accurate schemes with Riemann solvers), while the computational cost of numerical flux of KLWR (KLW) is about twice more expensive than that of HLLE. This is because the 2nd order accurate schemes using Riemann solvers require the computation of the numerical flux and the reconstruction twice during one time step (the second order accurate RK method).

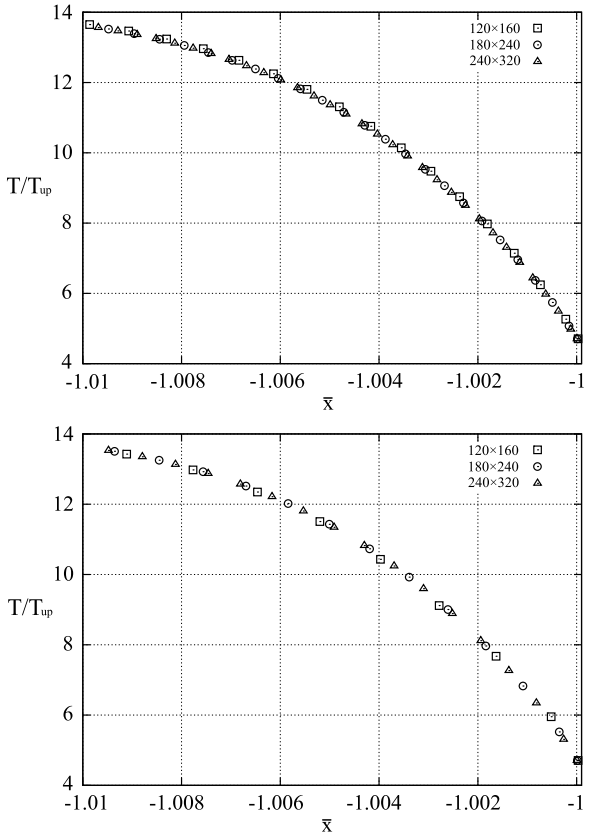


**Fig. 19.** The temperature distribution in the boundary-layer ($y = 0$). Upper: Mesh-A and lower: Mesh-B.

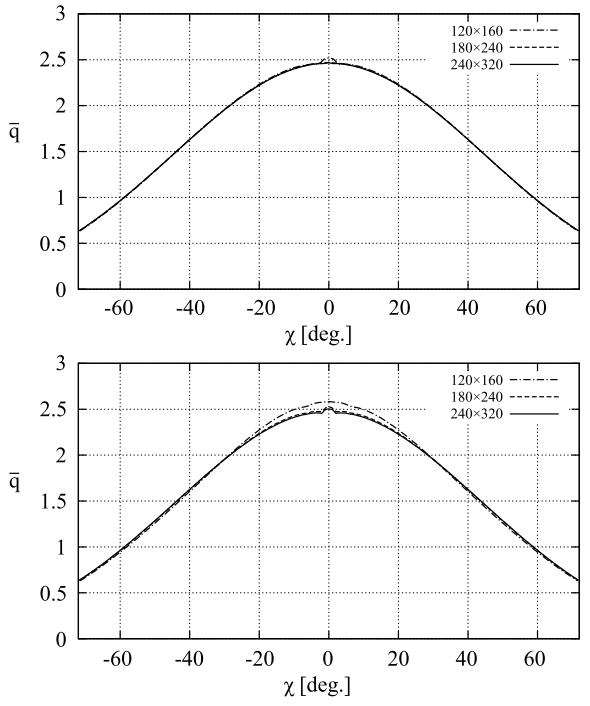


**Fig. 20.** The distribution of the heat flux along the cylinder surface. Upper: Mesh-A and lower: Mesh-B.

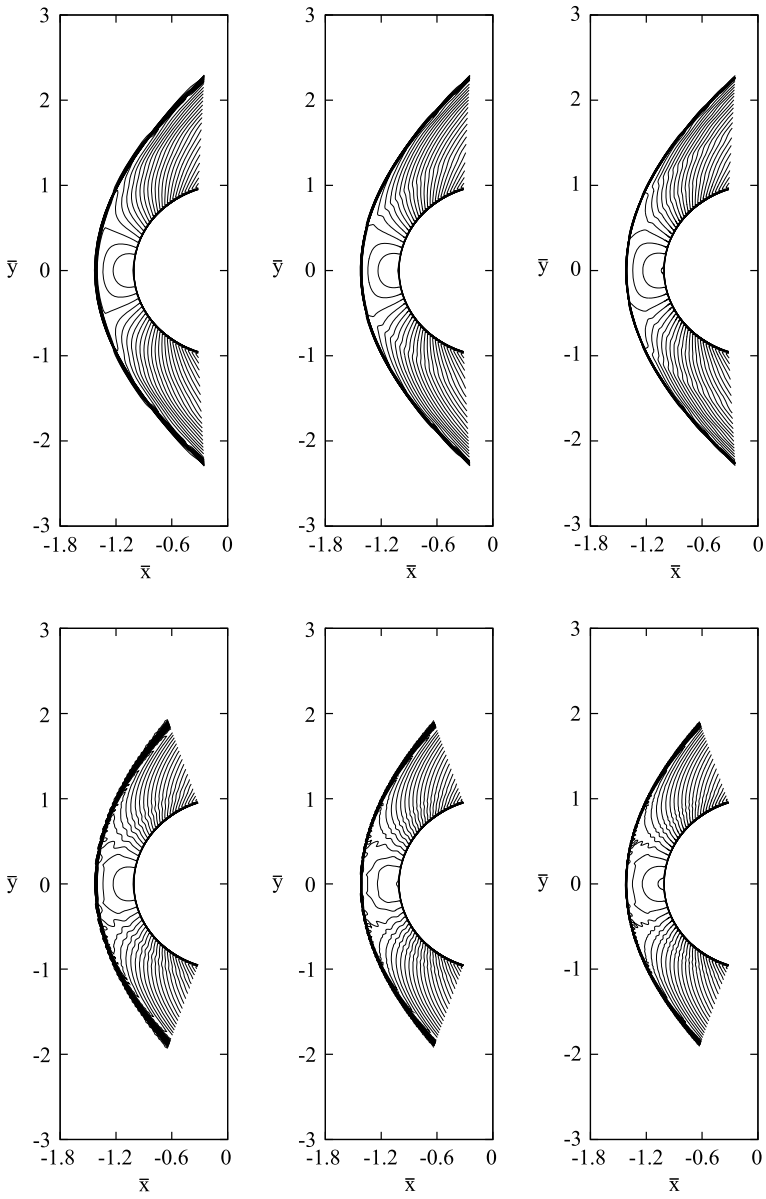


**Fig. 21.** Density fields for different mesh systems (hybrid of HLLE and HLLC with remedy). Upper: Mesh-A and lower: Mesh-B. Left: $(n_\xi, n_\eta) = (120, 160)$; middle: $(n_\xi, n_\eta) = (180, 240)$; and right: $(n_\xi, n_\eta) = (240, 320)$. The range of isolines is the same as in Fig. 18.

Finally, we briefly explain the performance of GKB in the present viscous flow problem for the same Mach number and the same Reynolds number; the technique of Prandtl number fix and the Sutherland formula are not employed, i.e. the Prandtl number is 1 and the viscosity is independent of the temperature; the collision time $\tau$ at cell-edge is given by Eq. (22) in Ref. [17], i.e.

$$\tau = \frac{\mu}{P^C} + \frac{|P^L - P^R|}{P^L + P^R}\Delta t, \tag{30}$$

where $\mu$ is the viscosity and $P^C = \rho^C T^C$; Mesh-A is employed in the computation. The onset of the carbuncle phenomenon is clearly observed, e.g. for $(n_\xi, n_\eta) = (120, 160)$ [$Asy = 2 \times 10^{-2}$ and $Res = 7 \times 10^{-5}$] and $(n_\xi, n_\eta) = (180, 240)$ [$Asy = 3 \times 10^{-3}$ and $Res = 10^{-6}$]. In the case of $(n_\xi, n_\eta) = (240, 320)$ the carbuncle phenomenon is nearly suppressed [$Asy = 8 \times 10^{-4}$ and *Res* effectively vanishes] but the post-shock wrinkles are clearly seen. As the remedy against these shock anomalies, the following procedure, which is similar to that in Section 4, is applied to GKB. The second term on the right hand side of Eq. (30) is recomputed in the same way as in the case of the jump indicator $\alpha$ and the slopes are suppressed according to

Eq. (27). The remedy also works very well; *Asy* and *Res* become effectively zero and shock anomalies disappear in all the above three cases.

## 6. Discussions

We have assessed the performance of the Lax–Wendroff scheme reinforced by Maxwellian and proposed a simple remedy against shock instabilities at the level of the preprocessing. The remedy suppresses the onset of shock anomalies quite satisfactorily in the problem of hypersonic flows past a cylinder for various cases of mesh system and resolution. A similar remedy also works for GKB, which is in contrast to the hybrid scheme of HLLE and HLLC. In the problem of a planar shock wave, however, even EFM exhibits the post-shock oscillations, though very small, when the grid alignment is poor. This implies that the robustness of KLWR demonstrated in the problem of hypersonic flows past a cylinder is brought by the synergy effect of the remedy and the intrinsic dissipation of the scheme. The latter contribution, however, decreases as the resolution increases and some shock instability will eventually rise up. The results of Section 3.1, i.e. Figs. 6, 13–15, imply that the disturbances can be suppressed to an acceptable level for practical purposes even in this case. In other words, the shocking title of Ref. [8] is very appropriate but shock instabilities can be easily treated especially in the case of KLW and GKB. The side-effect of the remedy appears as a slight increase in the thickness of the numerically captured shock wave and it is not clear at present whether the mitigation is possible or not. KLWR is capable of competing with shock-capturing schemes with Riemann solvers even for the computational efficiency.

As we have seen, very satisfactory results have been obtained owing to the robustness of kinetic schemes. Then, it is interesting to see whether kinetic theory essentially contributes to the robustness or not. For this purpose, we have carried out the computation of hypersonic inviscid flow past a cylinder (Section 3.3) using a simplified KLWR without any kinetic ingredients; the error function $\mathrm{erf}(x)$ and the exponential function $\exp(-x)$ in Eq. (A.5) of the appendix are replaced by the ad hoc functions $s_1(x)$ and $s_2(x)$ defined by

$$s_1(x) = \begin{cases} -1 & x \leqslant -1, \\ x & |x| < 1, \\ 1 & x \geqslant 1 \end{cases} \tag{31}$$

and

$$s_2(x) = \begin{cases} 1-x & 0 \leqslant x \leqslant 1, \\ 0 & 1 < x, \end{cases} \tag{32}$$

respectively, and $\hat{\boldsymbol{h}}^H$ in Eq. (A.9) is replaced by $\boldsymbol{h}^H$ $(H = L, R)$. The results of the simplified scheme are almost identical to those of the original KLWR; the computational cost is appreciably reduced. This suggests that kinetic theory does NOT essentially contribute to the robustness of kinetic schemes. It should rather be emphasized that kinetic approach presents a new artificial diffusion form of numerical flux. The robustness of the KLWR is brought from the numerical dissipation in $\boldsymbol{F}^D$ (see Eq. (A.8) in Appendix A). The formula of $\boldsymbol{F}^D$ in the simplified scheme is in the form

$$\boldsymbol{F}^D = \frac{1}{2}\left(\boldsymbol{\Phi}^L + \boldsymbol{\Phi}^R\right) + \frac{1}{2}\left(a^L\boldsymbol{\Phi}^L - a^R\boldsymbol{\Phi}^R\right) + b^L\boldsymbol{h}^L - b^R\boldsymbol{h}^R, \tag{33}$$

which has four control parameters $a^L$, $a^R$, $b^L$, and $b^R$. It becomes the standard central-upwind one for $a^L = a^R = A$ and $b^L = b^R = B/2$:

$$\boldsymbol{F}^{standard} = \frac{1}{2}\left(\boldsymbol{\Phi}^L + \boldsymbol{\Phi}^R\right) + \frac{A}{2}\left(\boldsymbol{\Phi}^L - \boldsymbol{\Phi}^R\right) + \frac{B}{2}\left(\boldsymbol{h}^L - \boldsymbol{h}^R\right). \tag{34}$$

HLLE belongs to this category and the Lax–Friedrichs and the local Lax–Friedrichs (Rusanov) schemes are categorized into its special case ($A = 0$). In the derivation of HLLE the functional forms of the two control parameters $A$ and $B$ are determined by a deep insight on the basis of the theory of nonlinear waves. Nevertheless, its robustness is poorer than the abovementioned ad hoc scheme. This also suggests that the theory of nonlinear waves is NOT indispensable for shock-capturing. It is, however, too hasty to conclude at present that the four control parameter approach is better than the two control parameter one. This topic, which is along with the context of how the theory of shock and boundary-layer capturing schemes can be simplified, is currently under our study.

## Appendix A

The explicit formulas of the numerical flux are given for the nondimensional compressible Euler equations in two space dimension $(x, y)$ without the component of the flow velocity in the $z$ direction ($w = 0$), i.e. Eq. (1) with $\tilde{\boldsymbol{h}} = (\rho, \rho u, \rho v, \rho[T/(\gamma-1) + (u^2+v^2)/2])^{\mathrm{T}}$ and

$$\boldsymbol{\Phi} = \begin{pmatrix} \rho u \\ \rho u^2 + P \\ \rho u v \\ [\frac{\rho T}{\gamma - 1} + \rho\frac{u^2+v^2}{2} + P]u \end{pmatrix}, \tag{A.1}$$

$$\boldsymbol{\Psi} = \begin{pmatrix} \rho v \\ \rho u v \\ \rho v^2 + P \\ [\frac{\rho T}{\gamma-1} + \rho\frac{u^2+v^2}{2} + P]v \end{pmatrix}. \tag{A.2}$$

The primitive variables are given by $\boldsymbol{h} = (\rho, u, v, T)^{\mathrm{T}}$. The numerical flux $\boldsymbol{F}$ is approximated in the form:

$$\boldsymbol{F} = \Delta t\big((1-\alpha)\boldsymbol{F}^C + \alpha\boldsymbol{F}^D\big) + \frac{(\Delta t)^2}{2}\boldsymbol{\Phi}_t. \tag{A.3}$$

The $\boldsymbol{F}^C$ and $\boldsymbol{F}^D$ are $\boldsymbol{\Phi}$ computed from $g_C$ and that done from $g_D$, respectively, and $\boldsymbol{\Phi}_t$ corresponds to $\partial\boldsymbol{\Phi}/\partial t$. The conservative variables $\tilde{\boldsymbol{h}}^C$ are computed from $g_D$ and the results are given by

$$\tilde{\boldsymbol{h}}^C = \frac{1+a^L}{2}\tilde{\boldsymbol{h}}^L + \frac{1+a^R}{2}\tilde{\boldsymbol{h}}^R + b^L\boldsymbol{d}^L - b^R\boldsymbol{d}^R, \tag{A.4}$$

where

$$a = \mathrm{erf}\left(\frac{u}{\sqrt{2T}}\right), \qquad b = \sqrt{\frac{T}{2\pi}}\exp\left(-\frac{u^2}{2T}\right), \tag{A.5}$$

and

$$\boldsymbol{d} = (0, \rho, 0, \rho u/2)^{\mathrm{T}}. \tag{A.6}$$

The primitive variables $\boldsymbol{h}^C = (\rho^C, u^C, v^C, T^C)^{\mathrm{T}}$ are readily computed from the conservative variables $\tilde{\boldsymbol{h}}^C$, e.g. $u^C = (\rho u)^C/\rho^C$. The $\boldsymbol{F}^C$ and $\boldsymbol{F}^D$ are given by

$$\boldsymbol{F}^C = \boldsymbol{\Phi}\big(\boldsymbol{h}^C\big), \tag{A.7}$$

$$\boldsymbol{F}^D = \frac{1+a^L}{2}\boldsymbol{\Phi}^L + \frac{1-a^R}{2}\boldsymbol{\Phi}^R + b^L\hat{\boldsymbol{h}}^L - b^R\hat{\boldsymbol{h}}^R, \tag{A.8}$$

where

$$\boldsymbol{\Phi}^H = \boldsymbol{\Phi}\big(\boldsymbol{h}^H\big) \qquad (H = L, R),$$

and

$$\hat{\boldsymbol{h}}^H = \boldsymbol{h}^H + \big(0, 0, 0, \rho^H T^H/2\big)^{\mathrm{T}} \qquad (H = L, R). \tag{A.9}$$

For the convenience in the expression of $\boldsymbol{\Phi}_t$, five matrices of $4\times 4$, the elements of which are functions of the primitive variables $\boldsymbol{h}$, are introduced:

$$\boldsymbol{L}(\boldsymbol{h}) = \begin{pmatrix} 0 & 1 & 0 & 0 \\ \frac{\gamma-3}{2}u^2 + \frac{\gamma-1}{2}v^2 & (3-\gamma)u & (1-\gamma)v & \gamma-1 \\ -uv & v & u & 0 \\ \frac{\gamma-2}{2}u(u^2+v^2) - \frac{\gamma u T}{\gamma-1} & \frac{1}{2}((3-2\gamma)u^2+v^2) + \frac{\gamma T}{\gamma-1} & (1-\gamma)uv & \gamma u \end{pmatrix}, \tag{A.10}$$

$$\boldsymbol{M}(\boldsymbol{h}) = \begin{pmatrix} u & \rho & 0 & 0 \\ T+u^2 & 2\rho u & 0 & \rho \\ uv & \rho v & \rho u & 0 \\ [\frac{\gamma T}{\gamma-1} + \frac{u^2+v^2}{2}]u & \frac{\gamma\rho T}{\gamma-1} + \frac{\rho(3u^2+v^2)}{2} & \rho uv & \frac{\gamma\rho u}{\gamma-1} \end{pmatrix}, \tag{A.11}$$

$$\boldsymbol{N}(\boldsymbol{h}) = \begin{pmatrix} v & 0 & \rho & 0 \\ uv & \rho v & \rho u & 0 \\ T+v^2 & 0 & 2\rho v & \rho \\ [\frac{\gamma T}{\gamma-1} + \frac{1}{2}(u^2+v^2)]v & \rho uv & \frac{\gamma\rho T}{\gamma-1} + \frac{\rho}{2}(u^2+3v^2) & \frac{\gamma\rho v}{\gamma-1} \end{pmatrix}, \tag{A.12}$$

$$\boldsymbol{W}(\boldsymbol{h}) = \begin{pmatrix} 1 & 0 & 0 & \frac{\rho}{2T} \\ u & 2\rho & 0 & 0 \\ v & 0 & \rho & \frac{\rho v}{2T} \\ \frac{\gamma+1}{2(\gamma-1)}T + \frac{u^2+v^2}{2} & \frac{3\rho u}{2} & \rho v & \frac{\rho}{4T}(\frac{3\gamma+3}{\gamma-1}T + v^2) \end{pmatrix}, \tag{A.13}$$

$$\boldsymbol{Z}(\boldsymbol{h}) = \begin{pmatrix} 0 & \frac{\rho v}{T} & 0 & -\frac{\rho u v}{2T^2} \\ v & 0 & \rho & \frac{\rho v}{2T} \\ 0 & \frac{\rho(T+v^2)}{T} & 0 & -\frac{\rho u(T+v^2)}{2T^2} \\ \frac{uv}{2} & \frac{\rho v}{2T}(\frac{3\gamma-1}{\gamma-1}T + v^2) & \frac{\rho u}{2} & -\frac{\rho u v}{4T^2}(\frac{\gamma+1}{\gamma-1}T + v^2) \end{pmatrix}. \tag{A.14}$$

Then $\boldsymbol{\Phi}_t$ in Eq. (A.3) is given by

$$\boldsymbol{\Phi}_t = -\boldsymbol{L}^C(\Delta\boldsymbol{\Phi} + \Delta\boldsymbol{\Psi}), \tag{A.15}$$

$$\Delta\boldsymbol{\Phi} = \frac{1+a^L}{2}\boldsymbol{M}^L\boldsymbol{h}_x^L + \frac{1-a^R}{2}\boldsymbol{M}^R\boldsymbol{h}_x^R + b^L\boldsymbol{W}^L\boldsymbol{h}_x^L - b^R\boldsymbol{W}^R\boldsymbol{h}_x^R, \tag{A.16}$$

$$\Delta\boldsymbol{\Psi} = \frac{1+a^L}{2}\boldsymbol{N}^L\boldsymbol{h}_y^L + \frac{1-a^R}{2}\boldsymbol{N}^R\boldsymbol{h}_y^R + b^L\boldsymbol{Z}^L\boldsymbol{h}_y^L - b^R\boldsymbol{Z}^R\boldsymbol{h}_y^R, \tag{A.17}$$

where $\boldsymbol{L}^C = \boldsymbol{L}(\boldsymbol{h}^C)$, $\boldsymbol{M}^H = \boldsymbol{M}(\boldsymbol{h}^H)$, $\boldsymbol{N}^H = \boldsymbol{N}(\boldsymbol{h}^H)$, $\boldsymbol{W}^H = \boldsymbol{W}(\boldsymbol{h}^H)$, and $\boldsymbol{Z}^H = \boldsymbol{Z}(\boldsymbol{h}^H)$ $(H = L, R)$. Incidentally, the matrices $\boldsymbol{L}$, $\boldsymbol{M}$, and $\boldsymbol{N}$ correspond to $\partial\boldsymbol{\Phi}/\partial\tilde{\boldsymbol{h}}$, $\partial\boldsymbol{\Phi}/\partial\boldsymbol{h}$, and $\partial\boldsymbol{\Psi}/\partial\boldsymbol{h}$, respectively, and $\Delta\boldsymbol{\Phi}$ and $\Delta\boldsymbol{\Psi}$ correspond to $\partial\boldsymbol{\Phi}/\partial x$ and $\partial\boldsymbol{\Psi}/\partial y$, respectively.

## References


[1] J.J. Quirk, A contribution to the great Riemann solver debate, Int. J. Numer. Methods Fluids 18 (1994) 555–574.
[2] R. Sanders, E. Morano, M.-C. Druguet, Multidimensional dissipation for upwind schemes: Stability and applications to gas dynamics, J. Comput. Phys. 145 (1998) 511–537.
[3] J.C. Robinet, J. Gressier, G. Casalis, J.M. Moschetta, Shock wave instability and the carbuncle phenomenon: same intrinsic origin?, J. Fluid Mech. 417 (2000) 237–263.
[4] M. Pandolfi, D. D'Ambrosio, Numerical instabilities in upwind methods: Analysis and cures for the carbuncle phenomenon, J. Comput. Phys. 166 (2001) 271–301.
[5] Y.-X. Ren, A robust shock-capturing scheme based on rotated Riemann solvers, Comput. Fluids 32 (2003) 1379–1403.
[6] M. Dumbser, J.-M. Moschetta, J. Gressier, A matrix stability analysis of the carbuncle phenomenon, J. Comput. Phys. 197 (2004) 647–670.
[7] H. Nishikawa, K. Kitamura, Very simple, carbuncle free, boundary-layer-resolving, rotated-hybrid Riemann solvers, J. Comput. Phys. 227 (2008) 2560–2581.
[8] V. Elling, The carbuncle phenomenon is incurable, Acta Math. Sci. Ser. B 29 (2009) 1647–1656.
[9] K. Kitamura, E. Shima, P. Roe, F. Ismail, Evaluation of Euler fluxes for hypersonic flow computations, AIAA J. 47 (2009) 44–53.
[10] K. Kitamura, E. Shima, Y. Nakamura, P.L. Roe, Evaluation of Euler fluxes for hypersonic heating computations, AIAA J. 48 (2010) 763–776.
[11] J. Li, Q. Li, K. Xu, Comparison of the generalized Riemann solver and the gas-kinetic scheme for inviscid compressible flow simulations, J. Comput. Phys. 230 (2011) 5080–5099.
[12] K. Huang, H. Wu, H. Yu, D. Yan, Cures for numerical shock instability in HLLC solver, Int. J. Numer. Methods Fluids 65 (2011) 1026–1038.
[13] S. Zhang, S. Jiang, C.-W. Shu, Improvement of convergence to steady state solutions of Euler equations with the WENO schemes, J. Sci. Comput. 47 (2011) 216–238.
[14] S.K. Godunov, A finite difference method for computation of discontinuous solutions of the equations of fluid dynamics, Mat.i Sb. 47 (1959) 271–306.
[15] D.I. Pullin, Direct simulation methods for compressible inviscid ideal-gas flow, J. Comput. Phys. 34 (1980) 231–244.
[16] J.C. Mandel, S.M. Deshpande, Kinetic flux vector splitting (KFVS) for Euler equations, Comput. Fluids 23 (1994) 447–478.
[17] K. Xu, A gas-kinetic BGK scheme for the Navier–Stokes equations and its connection with artificial dissipation and Godunov method, J. Comput. Phys. 171 (2001) 289–335.
[18] K. Xu, M. Mao, L. Tang, A multidimensional gas-kinetic BGK scheme for hypersonic viscous flow, J. Comput. Phys. 203 (2005) 405–421.
[19] T. Ohwada, S. Kobayashi, Management of discontinuous reconstruction in kinetic schemes, J. Comput. Phys. 197 (2004) 116–138.
[20] T. Ohwada, S. Fukata, Simple derivation of high-resolution schemes for compressible flows by kinetic approach, J. Comput. Phys. 211 (2006) 424–447.
[21] A. Harten, P.D. Lax, B. van Leer, On upstream differencing and Godunov-type schemes for hyperbolic conservation laws, SIAM Rev. 25 (1983) 35–61.
[22] B. Einfeldt, On Godunov-type methods for gas dynamics, SIAM J. Numer. Anal. 25 (1988) 294–318.
[23] E.F. Toro, M. Spruce, W. Spears, Restoration of the contact surface in the HLL-Riemann solver, Shock Waves 4 (1994) 25–34.
[24] E.F. Toro, Riemann Solvers and Numerical Methods for Fluid Dynamics: A Practical Introduction, Springer-Verlag, 1999.
[25] R.J. Leveque, Finite Volume Methods for Hyperbolic Problems, Cambridge University Press, 2002.
[26] T. Ohwada, On the construction of kinetic schemes, J. Comput. Phys. 177 (2002) 156–175.
[27] T. Ohwada, K. Xu, The kinetic scheme for the full-Burnett equations, J. Comput. Phys. 201 (2004) 315–332.
[28] M.-S. Liou, A sequel to AUSM, AUSM+, J. Comput. Phys. 129 (1996) 364–382.
[29] M.-S. Liou, A sequel to AUSM, part II: AUSM+-up for all speeds, J. Comput. Phys. 214 (2006) 137–170.
[30] E. Shima, K. Kitamura, On new simple low-dissipation scheme of AUSM-family for all speeds, AIAA Paper 2009-136, 2009.
[31] J.A. Fay, F.R. Riddell, Theory of stagnation point heat transfer in dissociated air, J. Aeronaut. Sci. 25 (1958) 73–85.